An experimental investigation of metamorphism induced microstructure evolution in a model cohesive snow

by Michael Quast Edens

A thesis submitted in partial fulfillment of the requirements for the degree of Doctor of Philosophy In Engineering Applied Mechanics Option
Montana State University

Abstract:
Data describing snow microstructure is needed in order to verify theoretical models and the results obtained from numerical simulation of related processes. Unfortunately, such data is almost non-existent. One area of snow science where this deficiency is having an impact is in studies of microstructure metamorphism. Typically theoretical metamorphism models treat snow as an aggregate of spherical ice-grains. Adequate data describing spherical ice-grain metamorphism is non-existent. The lack of data primarily stems from the fact that the observation and measurement of microstructure is accomplished via surface sections. The location and identity of several of the most important features must be deduced from the cross sectional information that is present in order to make appropriate measurements. In the past, doing this in a consistent and objective manner has not been very successful.

The problem of consistency and objectivity has been solved by automating the feature identification and measurement process. To do this a set of criteria have been developed which characterize the microstructure appearing on a surface section. These provide a consistent and objective method for locating bond and neck cross sections. In addition a new relation has been developed which provides a way of measuring average neck length.

To begin providing some of the microstructure data needed for metamorphism studies, an experimental investigation of microstructure induced microstructure evolution has been performed. Four sets of 12 spherical ice-grain compacts were allowed to undergo microstructure induced metamorphism at one of four temperatures (-2°C, -5°C, -10°C, -15°C) for a period of five weeks. At various intervals surface sections were prepared from these samples which were then photographed using a CCD camera. Microstructure analysis was conducted using a computer program which incorporates the automated identification and measurement processes just mentioned. Results presented include bond, neck, and grain growth over time.

An extensive set of new data, detailing microstructure evolution in spherical ice-grain compacts, is now available. It was obtained using automated identification and measurement procedures. The major problems regarding identification and measurement consistency and objectivity have been solved.

AN EXPERIMENTAL INVESTIGATION OF METAMORPHISM INDUCED MICROSTRUCTURE EVOLUTION IN A "MODEL" COHESIVE SNOW

by

Michael Quast Edens

A thesis submitted in partial fulfillment
of the requirements for the degree

of

Doctor of Philosophy

In

Engineering

Applied Mechanics Option

MONTANA STATE UNIVERSITY-BOZEMAN
Bozeman, Montana

May 1997

APPROVAL

of a thesis submitted by

Michael Quast Edens

This thesis has been read by each member of the thesis committee and has been found to be satisfactory regarding content, English usage, format, citations, bibliographic style, and consistency, and is ready for submission to the College of Graduate Studies.

Robert L. Brown _____ (Signature) 6/12/97 Date

Approved for the Department of Mechanical Engineering

Vic Cundy _____ (Signature) 5/16/97 Date

Approved for the College of Graduate Studies

Robert L. Brown _____ (Signature) 6/12/97 Date

STATMENT OF PERMISSION TO USE

In presenting this thesis in partial fulfillment of the requirements for a doctoral degree at Montana State University-Bozeman, I agree that the Library shall make it available to borrowers under rules of the Library. I further agree that copying of this thesis is allowable only for scholarly purposes, consistent with "fair use" as prescribed in the U.S. Copyright Law. Request for extensive copying or reproduction of this thesis should be referred to University Microfilms International, 300 North Zeeb Road, Ann Arbor, Michigan 48106, to whom I have granted "the exclusive right to reproduce and distribute my dissertation in and from microform along with the non-exclusive right to reproduce and distribute my abstract in any format in whole or in part".

Signature 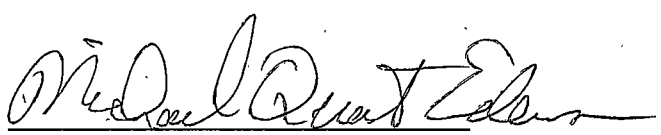

Date 6/13/97

TABLE OF CONTENTS

LIST OF TABLES

LIST OF FIGURES

ABSTRACT

Data describing snow microstructure is needed in order to verify theoretical models and the results obtained from numerical simulation of related processes. Unfortunately, such data is almost non-existent. One area of snow science where this deficiency is having an impact is in studies of microstructure metamorphism. Typically theoretical metamorphism models treat snow as an aggregate of spherical ice-grains. Adequate data describing spherical ice-grain metamorphism is non-existent. The lack of data primarily stems from the fact that the observation and measurement of microstructure is accomplished via surface sections. The location and identity of several of the most important features must be deduced from the cross sectional information that is present in order to make appropriate measurements. In the past, doing this in a consistent and objective manner has not been very successful.

The problem of consistency and objectivity has been solved by automating the feature identification and measurement process. To do this a set of criteria have been developed which characterize the microstructure appearing on a surface section. These provide a consistent and objective method for locating bond and neck cross sections. In addition a new relation has been developed which provides a way of measuring average neck length.

To begin providing some of the microstructure data needed for metamorphism studies, an experimental investigation of microstructure induced microstructure evolution has been performed. Four sets of 12 spherical ice-grain compacts were allowed to undergo microstructure induced metamorphism at one of four temperatures ($-2^{o}C$, $-5^{o}C$, $-10^{o}C$, $-15^{o}C$) for a period of five weeks. At various intervals surface sections were prepared from these samples which were then photographed using a CCD camera. Microstructure analysis was conducted using a computer program which incorporates the automated identification and measurement processes just mentioned. Results presented include bond, neck, and grain growth over time.

An extensive set of new data, detailing microstructure evolution in spherical ice-grain compacts, is now available. It was obtained using automated identification and measurement procedures. The major problems regarding identification and measurement consistency and objectivity have been solved.

CHAPTER 1

SNOW

1.1 Introduction

Seasonal snow is an essential part of our natural environment. Often we don't appreciate the impact it has on our lives. It can be a source of recreation and at the same time become a deadly avalanche. In many parts of the world, the water stored in snow packs is the primary source of water during the summer and autumn. Snow can have a large influence on the net exchange of solar radiation with the earth.

In the form of avalanches, snow may be responsible for millions of dollars lost each year, due to road closures, property damage, and destroyed forest land in the U.S. and Canada alone. Construction of highway avalanche sheds, diversions, dikes and barriers on avalanche paths above highways, villages and resorts are also extremely expensive as defensive measures. In terms of human costs, hundreds of lives are lost each year, with many more than that who are fortunate enough to be rescued alive.

These are some of the reasons that prediction and control of avalanches are important aspects of snow research. Knowledge of avalanche formation, snow strength, and those changes that may actually decrease their danger are some of the things needed for accurate prediction. Avalanche control, which may occur in the form of intentional initiation of ava-

lanches with the use of explosives and projectiles, or in the form of flow control through barriers, dikes, and diversions, requires knowledge of wave propagation in snow, factors influencing that, and the stresses produced by avalanches when impacting structures.

Snow also plays a crucial role in providing a continuous source of fresh water during spring and summer months. It accounts for over 1/3 of the water used world wide for irrigation (Stepphun 1981). Being able to predict the water runoff from mountain snow packs is important for effective regulation of dams and potential floods. Typically snow hydrologist want to know such things as time of melt, quantity and rate of water released, volume of water entering soil, and amount of evaporation. This requires a knowledge of how volumetric decrease in snow water equivalent is governed by such factors as snow melt, evaporation, condensation, and transmission of water to the soil (Male 1981).

Earth's climate is also influenced by snow through its emissivity, reflection, and the absorption of solar radiation (e.g. Berry 1981; Warren 1982; Dozier et al. 1987). A related area, which is of interest to the military, is radar interaction with snow cover (Mellor 1977).

Even though snow is a granular material, its behavior, properties and processes, often fall far outside those normally encountered in traditional studies of granular materials. One very unique property of snow is its high compressibility (Mellor 1977). Relative displacements in excess of 99% possible (Yosida 1963). Much of the temperature range of interest in snow studies, finds snow near its melting temperatures. As a result of its high compressibility and elevated temperatures, we are dealing with a highly non-linear, highly temperature dependent, granular material. The factor underlying all of this is snow's highly variable microstructure. Snow's mechanical (e.g. Yosida 1963; Hobbs 1965; Keeler

1969; Kry 1975a,b; Gubler 1978a,b; Brown 1979a,b; Hansen and Brown 1986,1987; Edens and Brown 1991, Brown and Edens 1991), thermodynamic (e.g. Kingery 1960; Yosida 1963; Hobbs and Mason 1964; Colbeck 1980, 1983,1993; Adams and Brown 1990; Adams and Sato 1993; Brown et al. 1994,1996,1997a,b), and electromagnetic (e.g. Warren 1982) properties and associated processes are all direct outcomes of its microstructure. Measurement of the material microstructure has long been a central goal of past research efforts (e.g. Yosida 1963; Hobbs and Mason 1964; Colbeck 1980; Brown et al. 1994,1996,1997a,b).

Considering the importance of microstructure, it would seem that significant progress in its characterization and measurement would have occurred. Yet, as should become clear by the end of this chapter, there is a definite lack of relevant microstructure measurements and still considerable work to be done in characterization. Much of this lack is due to difficulties inherent in characterizing and measuring snow's microstructure. In this thesis, it will be demonstrated that most of the factors which have hampered progress in microstructure measurement can be overcome. As will be shown in Chapter 4, microstructural characterizations, required for the measurement process, can be stated as a set of well defined criteria. They are stated in terms of an image transformation technique (skeletonization), reviewed in Chapter 3, which also provides the framework around which automation of the entire measurement process can be based (Chapter 3 and 4). Automation is accomplished in the form of computer software. That is demonstrated in Chapter 5 where it is used to analyze microstructural evolution of aggregates of spherical ice particles. The measurements presented in that chapter are based upon the material of Chapter 2.

The experimental portion of this thesis (Chapter 5) is concerned with microstructure metamorphism. The general importance of metamorphism and its influence on snow science as a whole was noted by Colbeck in a session summary from the 1995 workshop "Future Directions in Snow and Ice Research" (Brown and Dent: editors, 1995). The first part of this chapter looks at several aspects of metamorphism of dry snow microstructure. Issues regarding characterization of snow microstructure and its measurement are then presented in section 1.3. Finally, in section 1.4 the purpose of this thesis will be stated.

1.2 Snow Microstructure and Microstructure Metamorphism

Structurally, snow is a granular material. It may be either consolidated or loose. Consolidated (cohesive) snow is characterized by a continuous ice network, formed through cohesion between ice grains, to form a porous structure. One feature of this microstructure is that over a wide density range it is a relatively open self-supporting structure. It could be described as being akin to a tinker toy structure where the grains coincide with the tinker toy joint blocks and the interconnecting structure coincides with the connecting sticks. This is contrasted to most other granular materials which are more akin to what would be obtained by dumping tinker toy joints into a pile. Typically cohesive forms of seasonal snow have densities $0.05\ g/cm^3 \le \rho \le 0.65\ g/cm^3$. Porosities (pore volume fraction) may vary from as low as 0.20 to as large as 0.95. A loose or weakly bonded form of snow, depth hoar, is normally found with densities in the low to mid density range ($0.1\ g/cm^3 \le \rho \le 0.3\ g/cm^3$). Note that in polar and glacier regions, snow may be found with

densities reaching $\rho \approx 0.85\ g/cm^3$ (Mellor 1977), the cut off between snow and ice. At such densities all of the pores are isolated from one another.

The Role of Surface Area in Microstructure Metamorphism

Regardless of the type of microstructure possessed by snow it is a thermodynamically active material. This characteristic is primarily due to the fact that snow has a large relative surface area. Specific surface areas may be as large as 10,000 m^2/m^3. As a result, snow is always trying to reduce that area, thereby reducing its large free surface energy, and moving it closer to an equilibrium state (e.g. de Quervain 1963; Hobbs 1965). This surface energy and the high homologous temperature (T/Tm>0.9) at which snow is often considered leads to highly mobile water molecules. It is relatively easy for these to evaporate off of a grains's surface, travel through the pore space in vapor form, move along the surface due to surface diffusion, or migrate through the ice's molecular lattice (Hobbs 1965). These migratory molecules are redistributed by moving from high concentrations to regions of lower concentration. There they become bound to the ice surfaces, effectively redistributing some of the ice volume and producing a reduction in the overall surface area. That in turn leads to a reduction in total surface free energy of the system.

This process of surface reduction as the system tries to reach a minimum energy state is played out in several different ways, primarily determined by temperature and the presence or absence of a significant temperature gradient. Over burden pressure can be important (e.g. Maeno and Ebinuma 1983) but is not considered here.

Snow metamorphism processes are often categorized by mechanism and effect. Bond and neck growth are generally attributed to sintering (common in powder metallurgy and ceramics). Grain growth arises due to temperature gradients, in some cases density gradients (Adams and Brown 1990), and grain size variations (Brown et al. 1994). There is an additional process called melt-freeze cycling (not considered here). Temperature gradient phenomena are considered first.

Temperature Gradient Metamorphism

When temperature gradients are imposed over a snow pack (layers of different types of snow, each having its own characteristics) significant changes in grain shape, size, and strength may occur. Normally temperature gradients must be sufficiently large ($(\Delta T)/(\Delta z) > 10\ ^{\circ}C/m$, Adams and Brown 1990) and the pore space must be sufficiently interconnected. Under these conditions, depending upon temperature, grain size, and pore size (Adams and Brown 1990), rounded ("equilibrium form", Colbeck 1983) grains will become increasingly faceted. The degree and rate of this transformation depends upon density, temperature, temperature gradient, grain shape, and pore size (Colbeck 1983). Grains become more faceted at higher temperature gradients, while at low temperature gradients they are more rounded. Higher temperatures generally accelerate both processes. It is currently understood that most of the mass transport proceeds through both the pores by vapor diffusion and through the ice network by a process referred to as "hand to hand" diffusion (Yosida et al 1955, from Colbeck 1993). This process characterizes water vapor transport between coupled sources and sinks.

If the conditions are sustained long enough, grains can reach a form known as "depth hoar" (de Quervain 1963). It is a weakly bonded, highly faceted grain form. It may be found with hexagonally arranged facets and a cupped base.

According to Perla and Ommanney (1985), the influence of strong temperature gradients is highly dependent upon density. Their findings indicate that in low density newly fallen snow ($\rho \sim 0.1$ g/cm^3), evolution is towards large, weakly bonded, "depth hoar" crystals, while older snow ($\rho \sim 0.3$ g/cm^3) evolves toward smaller faceted grains in the form of prisms, forming a strong structure known as hard depth hoar.

Sintering and Geometry Driven Metamorphism

The initial form of metamorphism normally undergone by freshly fallen snow is called destructive metamorphism (de Quervain 1963). The snow flakes of fresh snow have large surface areas. A reduction of surface area and surface free energy occurs as the flake's branches decompose into individual fragments. These fragments undergo an additional change as the smaller fragments disappear, a result of mass being transferred to larger fragments. As the larger particles continue to grow at the expense of smaller ones, a gradual evolution toward rounded shapes, known as equilibrium forms (Colbeck 1983), occurs. As these grains come into contact they can obtain a net decrease in surface free energy if they adhere to one another (Kingery 1960), due to the removal of twice the area of contact.

The ensuing metamorphism, in the absence of a significant temperature gradient, is a process of bond and neck growth, called sintering (e.g. Kingery 1960; Kuriowa 1961;

Hobbs and Mason 1964; Maeno and Ebinuma 1983). In the absence of external pressures, four mechanisms for transporting mass to the neck regions usually occur: 1) vapor diffusion through evaporation-condensation, 2) surface diffusion through concentration gradients along the neck region and due to surface tension forces, 3) volume diffusion by molecular migration along vacancies in the ice lattice, and 4) viscous and plastic flow of material in the neck regions due to surface tension forces (e.g. Kingery 1960; Kuriowa 1961; Hobbs and Mason 1964; Maeno and Ebinuma 1983). These mechanisms are assumed to be governed by process which conform to equations of the general form

$$\left(\frac{r_b}{r_g}\right)^n = \frac{B(T)}{r_g^m} t,$$

where r_b is the bond radius, r_g is the grain radius, $B(T)$ is a temperature dependent coefficient, t time, and m, n are integers determined by the particular transport mechanism. Early debate on this occurred with regard to the dominant transport mechanism. Kingery (1960) indicated that surface diffusion is a dominant mechanism, while Kuriowa (1961) proposed volume diffusion, and Hobbs and Mason (1964) claimed vapor diffusion was the dominant process. Resolution of this question did not happen until the work of Maeno and Ebinuma (1983). They showed, using pressureless sintering diagrams, that vapor diffusion and surface diffusion were dominant, depending upon the ratio r_b/r_g and T/T_m (grain size and temperature).

There is one other driving mechanism that has been considered by several researchers. It is often referred to as "equi-temperature" metamorphism, which as Colbeck (1980) points out, is a misnomer, and that it should be called something like "grain curvature-metamorphism". As the last name suggests this type of metamorphism is concerned with

how variations in surface curvature affect metamorphism. Surface curvature produces a vapor pressure gradient along the surface. Lower pressures are associated with the concave necked regions (relative to the ice) and higher pressures occur over the convex surfaces (Colbeck 1980, Brown 1994). Findings indicate that when r_b/r_g is small, this effect may dominate, as long as there is no overriding temperature gradient. The relative bond growth equations for the two dominant sintering mechanism, given by Maeno and Ebinuma (1983), demonstrate how curvature effects may dominate the early stages of sintering. The general form of the growth equations given is

$$\frac{r_b}{r_g} = \frac{A(T)}{r_g} K_1^n \quad \text{(n=2, vapor transport; n=3, surface diffusion)}$$

where

$$K_1 = \left(\frac{2}{r_g} + \frac{1}{r_b} - \frac{1}{r_n}\right)\left(1 - \frac{r_b}{r_g}\right)$$

and $A_n(T)$ is an appropriate temperature dependent coefficient. Curvature effects are produced by the K_1 where $1/r_g$ is the average grain curvature and $1/r_n$ and $1/r_b$ are the two principal neck curvatures (one parallel to the bond, $1/r_b$, and the other perpendicular to that $1/r_n$).

The work of Brown et al. (1994) is important in that both sintering and radius of curvature metamorphism were accounted for. Brown also demonstrated in a numerical simulation the effects of relative grain growth on grain size, deposition rates along the neck, vapor velocities along the neck, as well as the effects on bond growth due to decrease in source-grain size. Though there was an associated experimental study, also using spherical

particles, some of the necessary measurement techniques were not available. The experimental results presented were inadequate to verify the analytical and numerical calculations.

Since their last study, Brown et al. (1996, 1997a,b), developed a mixture theory formulation of ET metamorphism. It models the material as a distribution of particle sizes, simultaneously, where each group of particle sizes are treated as a separate phase. An accompanying numerical simulation was presented which examined a system with five distinct grain sizes (initial condition). Two different distributions of these 5 particle sizes were evaluated, one based upon initially equal numbers and the other based upon initially equal volume fractions. In both cases, as consequence of the growth of larger particles, there was a reduction in the number of small particles. The rate at which particle size-distributions changed and the manner in which those changes occurred, were shown to be dependent upon the initial material microstructure.

Unfortunately, virtually no experimental data which documents changes in microstructure during metamorphism exists. Other than the partial results presented in Brown et al. (1994) and the measurement of bond radius for individual pairs of equal size spherical ice grains (Kingery 1963), no relevant experimental studies, providing measurements of microstructure parameters as they change over time and at different temperatures, are available. Though the theoretical and numerical results give results qualitatively similar to a few experimental investigations of natural snow involving microstructure measurements (e.g. Keeler 1969; Kry 1975a,b; Gubler 1978a,b; Good 1975, 1989; Good and Krusi 1992), it is essential that an experimental study be conducted with grains corresponding to

those assumed in the theory. Only in that way can the physics of the theory be validated without concern for such things as the effects of grain shape.

1.3 Measurement of Snow Microstructure

Historically, the tools and technology available for measuring snow microstructure have been inadequate, so much so that even the ability to characterize microstructure has been adversely affected. In this section a brief discussion of microstructure measurement is presented.

Two of the most common methods by which microstructure is observed are thin sections, which are thin partially transparent slices (thickness <30 μm, Good 1975)and surface sections, which are opaque plane cross sections (Kry 1975a; Perla 1982; Perla et al. 1988). Thin sections tend to be both difficult to make and time consuming (Kry 1975a). Because they are not single planes, their analysis using Stereology (Chapter 2) presents additional difficulties not encountered with true plane sections. They do have the advantage that (Perla 1985; Dozier et al. 1987) grain boundaries may be visible when sections are viewed with polarized light. For geometric characterization, plane sections offer simpler preparation techniques, faster preparation, and more straight forward analysis when using stereology. However, surface sections also present problems. Sample preparation is also labor intensive, and often grain/pore interfaces are not clearly defined. These interfaces also tend to migrate due to ice sublimation when the surface section is exposed to the air. One of the biggest obstacles to overcome in microstructure measurement, when using

stereology, is characterizing microstructure in such a way that it is amenable to measurement, via stereology. Referring back to the last section, we see that the preferred geometric parameters include mean values for the size of such things as grains, bonds, necks, and pores. Number densities, for example number of bonds per volume, are also important.

Kry (1975a) appears to be the first snow researcher to really exploit the potential of stereology to infer three dimensional parameter values from two dimensional measurements. In that important work he introduced an operational definition of a bond, describing it as it would appear on a surface section. He also showed how an existing stereology relation could be used to relate those bonds on the section plane to a mean 3D bond radius (assumed circular disk shaped bonds) and area. Bonds and grains are really complementary geometric features of an ice network microstructure. By defining bonds as they appear on a section plane, Kry presented a working definition of grain cross sections. With this work, he overcame one of the major hurdles of microstructure parameter evaluation. His methods were then applied to a study of viso-elastic properties and their relation to microstructure (Kry 1975b). A very strong case for the dependence of visco-elastic properties on mean bond radius, bond area, and neck length were made.

A modified form of Kry's bond location criteria was used by Gubler (1978b) in a study to determine the relationship between stereology parameters and tensile strength of snow. An important contribution of this paper was a procedure by which 3D coordination numbers could be obtained from distributions of 2D coordination numbers (number of bonds per grain). A strong correlation between 3D coordination number and strength was found. One problem associated with Gubler's method was an apparent lack of self-constancy. That was remedied by Hansen (1985).

To examine changes in microstructure when snow undergoes large deformations, Edens (1989; Edens and Brown 1991; Brown and Edens 1991) developed a semi-automated software package for snow surface section analysis. It used Kry's (1975a) bond identification criteria (applied visually). An attempt was also made to measure changes in neck length. Coordination numbers were estimated using software developed by Hansen (1985) and was based upon his modifications of Gubler's (1978b) procedure. Though successful in measuring most microstructure parameters of interest, neck length proved to be unsuccessful.

Though it may appear that progress in microstructure characterization and measurement have been adequate, major problems still exist. As stated, the Kry bond criteria has an unfortunate ambiguity, namely what is meant by grain size. Gubler's criteria is no better since it uses the term "obvious" as a major quantifier. Even more troubling is that, ambiguities aside, both methods are difficult to apply objectively and consistently, since previous procedures have not afforded a non-visual inspection-based approach to criteria application (Dozier et al. 1987). Dozier et al. (1987) were reserving judgment on the usefulness of the Kry-Gubler bond criteria, pending improvements in technology. Edens (1989) also found the lack of objectivity and consistency associated with visual-inspection to be problematical. They were implicated as being a major contributor to the unsuccessful attempts to measure changes in neck length.

The above discussion describes the current state-of-the-art in the use of stereology to measure microstructure. Progress in stereology and mathematical morphology as applied to materials science has continued (e.g a nice review by Liu 1993). But the type of devel-

opments needed to remedy the bond-neck objectivity problem do not appear to have been solved as far as the author has been able to determine.

1.4 The Current State of Snow Mechanics and Snow Physics

At the 1995 workshop on "Future Directions in Snow and Ice Research", attendees of the snow portion (many of the top snow researchers in the world) generally agreed, as outlined in the final report (Brown and Dent 1995) that future progress in snow mechanics and snow physics hinges upon an ability to measure microstructure and to relate microstructure to macroscopic processes and behavior. With that and the presentation of the previous sections, it is time to describe the purpose of this thesis.

1.5 Purpose of this Work

Most of the previous microstructural analyses have been conducted for the purpose of relating mechanical loading properties and deformation to microstructure. Similar studies for snow metamorphism are sorely lacking. It ought to be apparent that even if relevant experiments were run, problems in measurement would still need to be overcome.

With the critical need for data regarding microstructure and metamorphism, particularly for compacts of spherical particles (see end of section 1.3) the purpose of this thesis can be stated as follows:

1) Develop a procedure which will allow objective and consistent identification of sectioned bonds and necks,

2) to show that well defined criteria can be stated, thereby removing the ambiguities present in the Kry-Gubler (Kry 1975a; Gubler 1978b) criteria, as well as the criteria used by Edens (1989) to identify sectioned necks,

3) provide crucial data on microstructure evolution of spherical ice particle compacts ("model snows") due to microstructure metamorphism.

Chapter 2 provides an overview of pertinent procedures, terminology, and relationships of stereology. The foundation of objectives 1 and 2 above is called skeletonization. Definitions and algorithms are presented in Chapter 3. Chapter 4 is devoted to development of bond and neck identification criteria. Results and analysis of the experimental study in objective 3 are presented in Chapter 5. A conclusion and suggestions for further research conclude this thesis (Chapter 6).

CHAPTER 2

STEREOLOGY

In Chapter 5, snow microstructure evolution is examined. Measurements will be needed in order to evaluate 3-D microstructural parameters, which characterize the materials current microstructural state. Observations and measurements will be limited to those obtainable from plane sections cut through the microstructure. From section planes it is possible to obtain, counts, lengths, and area measurements. Immediately we see that some disparity exists between what can be measured and what we wish to measure. Fortunately, this doesn't necessarily preclude one from inferring useful information about 3-D microstructure from lower dimensional measurements.

Stereology methods provide the mathematical tools necessary for going from zero (counts), one (lengths), or two (area) dimensional measurements of a microstructure, to associated 3-D parameters of the microstructure itself. Statistical methods are required since the method in which measurements are made is in essence the same as sampling the microstructure under study. The theoretical relationships between sample geometries and the structural geometry follow from Geometric Probability (Kendall and Moran 1963) and Integral Geometry (Santaló 1976).

The purpose of this chapter is to outline those aspects of stereology that will be needed in the remainder of this thesis. Derivations of specific relations will not be given here.

Detailed discussions of stereology can be found in excellent texts by Dehoff and Rhines (1968), Underwood (1970), and Weibel (1980), among others.

The organization of this chapter is as follows. Terminology, concepts, and basic measurements are examined in section 2.1. Those fundamental stereology formulae which will be used later are presented in section 2.2. Particle volume measurement follows in section 2.3. In section 2.4 stereology of circular disks is presented. Finally, in section 2.5 edge effects and other measurement details are considered.

2.1 Terminology, Concepts, and Basic Measurement

Basic Statistical Relationships

This section gathers together those statistical relations which will be used throughout this thesis (see e.g. Mandel 1984).

Associated with a random variable is a probability distribution or frequency distribution. A random variable is a variable that is subject to chance or random fluctuations. The sequence of possible numerical outcomes assumed by a discrete random variable x during an experiment are denoted by $x_1, x_2, x_3, \ldots$. Associated with each possible outcome x_i is a probability value p_i. This association is determined by the probability distribution.

Because there may be many outcomes associated with an experiment, a way is needed to quantify those outcomes in terms of single typical value. The average is commonly used for this. A mathematically more precise term is the *Expected Value* (mean). The expected value associated with the discrete random variable x is expressed by:

$$E(x) = \sum_i x_i p_i .$$

This is also known as the first moment of the random variable x. The kth moment of the random variable x is given by:

$$E(x^k) = \sum_i x_i^k p_i$$

It is also useful to know the dispersion of outcomes about the expected value. This is normally measured with the variance. It is given by

$$Var(x) = \sum_i (x_i - E(x))^2 p_i .$$

This may also be expressed in terms of its square root, also known as the standard deviation, $\sigma(x) = \sqrt{Var(x)}$. A measure of dispersion relative to the expected value is called the coefficient of variation, $CV(x)$, and is given by:

$$CV(x) = \sigma(x)/E(x) \quad .$$

Because an experimenter can not usually make as many measurements as there are possible outcomes to an experiment, a subset (sample) of all the possible outcomes (population) is actually obtained. With the subset of values actually measured, it is desired to estimate both the expectation value and standard deviation associated with a population. If a random sample, $x_1, x_2, \ldots, x_n$, of size n is taken from some population, estimates of the population mean and standard deviation are:

$$estimate(E(x)) = \bar{x} = \frac{1}{n}\sum_{i=1}^{n} x_i , \qquad (1)$$

and

$$estimate(\sigma(x)) = S(x) = \sqrt{\frac{1}{(n-1)}\sum_{i=1}^{n}(x_i - \bar{x})^2}. \quad (2)$$

$\bar{x}$ is the sample average and $S(x)$ is the sample standard deviation. The reason for the divisor of $S(x)$ being $n-1$ rather than n is that there are only $n-1$ independent quantities in the equation.

Later we will have use for another type of average called the weighted average. Given a set of weights $\{w_1, w_2, ..., w_n\}$ corresponding to a sample $x_1, x_2, ..., x_n$, the weighted average is given by:

$$\overline{x_w} = \left(\sum_{i=1}^{n} w_i x_i\right) \Big/ \sum_{i=1}^{n} w_i. \quad (3)$$

The subscript indicates that the average is of the weighted variety. Note that equation (1) is recovered upon letting $w_i = 1$. The kth moment is given by:

$$\widehat{x^k}_w = \left(\sum_{i=1}^{n} w_i x^k{}_i\right) \Big/ \sum_{i=1}^{n} w_i. \quad (4)$$

The sample standard deviation for the weighted average is given by (see e.g. Mandel 1984)

$$\sigma_w(x) = \sqrt{\sum_{i=1}^{n}(x_i - \overline{x_w}^2)w_i} \Big/ \sqrt{\sum_{i=1}^{n} w_i}. \quad (5)$$

There are two measures of error that are also needed later. The first is called the standard error of the mean. Let $x_1, x_2, ..., x_n$, be a random sample of size n from some population with variance $v(x)$. It can be shown that (e.g. Mandel 1984) the variance of the sample average is related to the population variance by:

$$Var(\bar{x}) = \frac{Var(x)}{n}.$$

The relation is exact. The standard error of the sample average is the square root of this,

$$SE(\bar{x}) = \sigma(x)/\sqrt{n}. \tag{6}$$

Finally, if the standard error is divided by the sample average $\bar{x}$, the coefficient of error

$$CE(\bar{x}) = SE(x)/\bar{x} \tag{7}$$

is obtained. It is just the relative standard error of the sample average.

Microstructure and Phases

In this thesis, structure (internal or micro), refers to a specific spatial arrangement of particles (ice-grains) which comprise consolidated snow. The collection of these particles will be referred to as the *grain phase* g. These interconnected ice grains produce a continuous network of ice. This ice network or ice matrix, will be referred to as the *ice phase* $\imath$. Associated with an ice matrix is a complementary porous microstructure, called the pore phase. This is the portion of a volume of consolidated snow, not comprised of ice. It is occupied by one or more fluids, usually air and/or water. The pore phase will be designated by π. The space containing the specimen under study, the reference space, will be denoted by X.

The spatial arrangement of grains observed in consolidated snow arise when initially discrete particles are brought into contact. At points (or areas) of contact between these grains, a thermodynamic process called sintering occurs. The result of this process is that between each pair of particles in contact a solid connection is formed. The collection of

these connections are referred to as the bond phase, b. An additional phase designator, called the neck phase, η, will also find use. Details are presented in Chapter 4.

When referring to an arbitrary individual component of a particular phase, that phase designator will be subscripted by i. Again, the primary phase designators are, 1) g for the grain phase, 2) ι for the ice phase, 3) π for the pore phase, 4) b for the bond phase, and 5) η for the neck phase.

Microstructure observations are made with "probes". These probes are zero, one, or two dimensional geometric objects. That is, points, lines, or planes. It is common practice to arrange a number of probe elements into an array or grid. This arrangement is referred to as a *test system.* At the outset it is assumed that test a system's size and shape are known. To make a measurement, we can imagine placing a test system within a reference space X which contains a phase Φ of interest. A part of the test system may lay within Φ. The set of geometric objects formed by this intersection, between the test system and phase Φ, will be referred to as either *profiles* or *traces*. Individual profiles fall into one of three categories, point, lineal, or area and depend upon probe and object geometries.

When measurements in X are made with a point probe (set of P points), that probe will be denoted by $P(X)$, or, when there is no problem with ambiguity, by P. For a system of test lines in X (set of lines having a total length L) that probe will be designated as either $L(X)$ or L. Similarly, systems of test planes in X are denoted by either $A(X)$ or A (total area of planes in X is A).

Elements of a point grid which intersect a phase Φ will be denoted by P_Φ. Profiles from this intersection are points.

When the boundary (surface in three dimensions, plane curve in two dimensions) of Φ is intersected by a test line, a point profile is generated. The set of such intersection will be denoted by $I(\Phi)$ (using Weibel's notation, 1980). A lineal profile is generated by a test line when it intersects either an area in two dimensions or a volume in three dimensions. The total length of such profiles, for a phase Φ, is $L(\Phi)$. $N(\Phi)$ is the number of individual profiles having the same dimension as the probe that generated them (not for point probes though). In this case it is the number of lineal profiles generated by a line probe.

Planar probes can generate three profile geometries. Points, $I(\Phi)$, result when a plane intersects any lineal structure. A plane probe intersecting a surface or interface produces lineal traces, $B(\Phi)$. In the case of a planar probe intersecting a volume Φ, an area profile $A(\Phi)$ (cross section area of volume Φ) results. As with line probes and lineal profiles, $N(\Phi)$ is, in conjunction with planar probes, the number of area profiles.

These profile measurements are usually combined with a measure of the test system's size to give a density (not to be confused with a mass density). This is a natural representation since many of the features of interest are dispersed throughout a material's microstructure and therefore have a natural size measure represented by a density. The notation and form of these densities are defined below and are followed by some examples to help explain them.

For a point probe measure, the point fraction,

$$P_P(\Phi) = \frac{P(\Phi)}{P(X)}.$$

is used. It is just the ratio of the number of test points intersecting phase Φ and the total number of test points.

Three line probe densities are in common use. The number of point profiles of a boundary Φ per unit length of test line, is

$$I_L(\Phi) = \frac{I(\Phi)}{L(X)},$$

the length fraction of test line L intersecting phase Φ, is

$$L_L(\Phi) = \frac{L(\Phi)}{L(X)},$$

and the number of lineal phase Φ profiles per unit length of test line, is

$$N_L(\Phi) = \frac{N(\Phi)}{L(X)}.$$

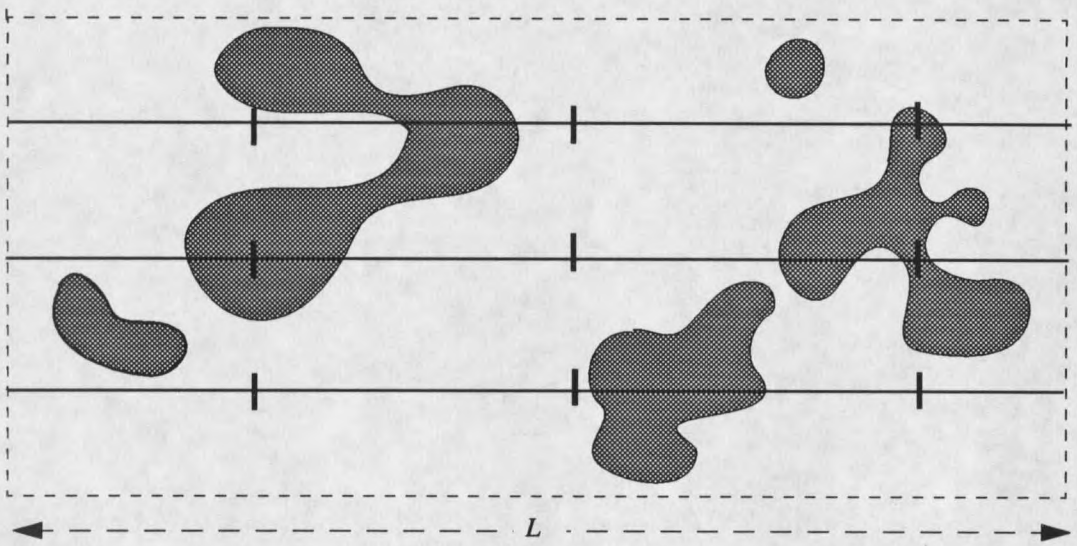

Figure 1. An example of probe measurements. 9 test points in the reference space (intersections of vertical and horizontal lines) intersect the gray-phase 3 times to give a point fraction $P_P(gray) = 3/9$. Three test lines, each of length L, intercept the gray-phase boundary, black curves, 12 times to give $I_L(black) = 12/3L$ for the number of point profiles per unit length of test line. There are 6 grey-phase linear profiles from the three line probes, giving $N_L(gray) = 6/3L = 2/L$ as the number of linear profiles per unit prove length. Within the dashed area A there are 5 grey-phase area profiles, which gives $N_A(gray) = 5/A$ for the number or area profiles per unit area.

There are two area densities that we will need. They are the number of area profiles per unit probe area

$$N_A(\Phi) = \frac{N(\Phi)}{A(X)},$$

and the area fraction

$$A_A(\Phi) = \frac{A(\Phi)}{A(X)}.$$

It should be noted that several other area densities are possible and that only those of immediate use have been presented.

Image Sampling

Specimen sampling is always accomplished via plane sections. Often measurements are made within sub-regions (quadrats) (Miles 1972) of a section plane. Generally, probes must have orientations which are isotropic with respect to the microstructure, if one is to avoid introducing any orientation bias. That is, orientation invariant measurements are required. To avoid bias due to probe positioning, a test system's origin should be placed according to a uniform-random distribution. The result is translation invariant measurements. Uniform-random imposes spatial homogeneity between probe and specimen. There are a number of ways of guaranteeing that sampling probes satisfy these requirements (see e.g. Miles and Davy 1975; Miles 1978; Gunderson 1981). If the microstructure under study is sufficiently isotropic and homogenous, probe application can be simplified considerably (Miles and Davy 1975; Miles 1978; Karlsson and Cruz-Orive 1991). All that is required is arbitrary placement of sampling probes, i.e. without reference to the micro-

structure. Snow, especially when a specimen has been subjected to little or no temperature gradient or deformation, exhibits a high degree of isotropy and homogeneity (Kry 1975a). For the purposes of this thesis, isotropy and homogeneity will be assumed, whenever stereology measurements are considered.

These assumptions do not eliminate bias (systematic errors) completely. Ratio estimates, in which the denominator is a random variable, exhibit some statistical bias (Cochran 1977). In practice this is usually small and can be ignored. As done by Karlsson and Cruz-Orive (1991), "unbiased" will mean "unbiased for all practical purposes".

2.2 Stereology Formulae

In this section we are interested in the parameters V_V, the volume fraction, S_V, the surface area to volume ratio, and L_3, the mean 3-D intercept length. These are very general parameters, since no assumptions about object shape are needed.

Volume Fraction V_V

Given a specimen X of volume $V(X)$, composed of several phases, one can specify the fraction of $V(X)$ occupied by any phase Φ_i, by its volume fraction, $V_V(\Phi_i)$. This fraction is given by

$$V_V(\Phi_i) = \frac{V(\Phi_i)}{V(X)}.$$

Any set of phases in X satisfy $\sum V_V(\Phi_i) \leq 1$. Equality holds when the material is saturated (Underwood 1970).

Estimates of volume fraction can be made using any of the three fraction probes discussed in the last section. A simple relation exists between these probe measurements and volume fraction. It is (e.g. Dehoff & Rhines 1968, Underwood 1970, Weibel 1980)

$$V_V(\Phi_i) = A_A(\Phi_i) = L_L(\Phi_i) = P_P(\Phi_i). \tag{8}$$

Volume fraction will be used as a parameter in other stereology formulae and in estimating specimen density. For snow density, it is reasonable to assume that a specimen is composed of two phases, air and ice. If V_S is the volume of a snow specimen, its density ρ_S can be expressed in terms of the volume fractions and densities of air and ice through the relation

$$\rho_S = \rho_a V_V(a) + \rho_\iota V_V(\iota).$$

$V_V(a)$ and $V_V(\iota)$ are the volume fractions of air and ice, respectively. Their corresponding material densities are denoted by ρ_a and ρ_ι. Because the density of air is much-much less than that of ice, the contribution of air can be neglected, so that $\rho_S \cong \rho_\iota V_V(\iota)$.

Surface Area to Volume Ratio S_V

In a multi phase material, one phase is separated from all others by an inter-phase interface, which for most purposes is just each phase's bounding surface. Discrete objects within a phase are also separated from one another by their individual bounding surfaces.

Knowledge of the density of this surface area is quite important. Its density may be expressed in two ways, surface area of Φ, per unit specimen volume, $V(X)$,

$$S_V(\Phi) = \frac{S(\Phi)}{V(X)},$$

or surface area $S(\Phi)$ of Φ per unit volume $V(\Phi)$ of Φ,

$$S_{V\Phi}(\Phi) = \frac{S(\Phi)}{V(\Phi)}.$$

In the last expression a reference space other than X was used. The alternate reference space, in this case Φ, was noted in the subscript. This practice will be followed throughout this thesis.

The first of these forms is determined by the stereology relation (e.g: Weibel 1980; Underwood 1970)

$$S_V(\Phi) = 2I_L(\Phi). \tag{9}$$

$I_L(\Phi)$ is the number intercepts of interface Φ per unit length of test line. Notice that for a material with only two phases, Φ_1 and Φ_2, since they share the same interface, then it follows that $I_L(\Phi_1) = I_L(\Phi_2)$. And, as a result $S_V(\Phi_1) = S_V(\Phi_2)$. The second form of the ratio is given by (Underwood 1970):

$$S_{V\Phi}(\Phi) = \frac{\bar{S}(\Phi)}{\bar{V}(\Phi)} = \frac{S_V(\Phi)}{V_V(\Phi)} = \frac{2I_L(\Phi)}{L_L(\Phi)}. \tag{10}$$

The last equality follows from equations (8) and (9). Equations (9) and (10) are valid for any mixture of surfaces in space, provided all surface intercept directions have equal probability of occurring (Weibel 1980).

In snow science the average coordination number $\bar{n}_3$, (mean number of bonds per grain), is an important parameter appearing in both mechanical and thermodynamic models. It is given by:

$$\bar{n}_3 = \frac{2N_V(b)}{N_V(g)}, \tag{11}$$

where $N_V(b)$ is the number of bonds per unit specimen volume, and $N_V(g)$ is the number of grains per unit specimen volume. Without specifying shapes, there is no way of estimating these two densities from a single section plane. Even if one can accurately specify shapes, there are still problems. The main one is a consequence of particle profile counting. Small profiles may not be easily identified, since resolution may not be sufficient to see small features in a section plane. The result may be a significant under-count. Because of the limitations inherent in identifying bonds on a single section, there will almost certainly be an under-count, and not necessarily due to grazing or small profile hits. Less sensitive to these difficulties are corresponding measurements of S_V. This can be used to define a bond density per unit grain surface area, which should exhibit less bias.

We start with equation (11). First, multiply both sides of the equation by the average cross-sectional bond area $\bar{A}(b)$. Then upon dividing by the average surface area per grain $\bar{S}(g)$, the expression

$$\frac{\bar{A}(b)\bar{n}_3}{\bar{S}(g)} = \frac{2N_V(b)}{N_V(g)}\frac{\bar{A}(b)}{\bar{S}(g)} \tag{12}$$

is obtained. The total bond surface area per sample volume, $S_V(b)$, is given by the numerator on the right hand side. The denominator is the total grain surface area per sample vol-

ume, $S_V(g)$. It is the sum of the total free ice surface area per sample volume, $S_V(\imath)$, and $S_V(b)$ i.e. $S_V(g) = S_V(\imath) + S_V(b)$. Now, substituting into equation (12) gives

$$\frac{\bar{A}(b)\bar{n}_3}{\bar{S}(g)} = \frac{S_V(b)}{S_V(g)} = \frac{S_V(b)}{S_V(\imath) + S_V(b)} = C_g. \tag{13}$$

C_g is called the contiguity (Gurland 1958). It is the average fraction of grain surface area shared with all neighboring grains. The density of bonds per unit grain surface area, N_{3S}, is obtained upon dividing equation (13) by $\bar{A}(b)$;

$$N_{3S} = \frac{C_g}{\bar{A}(b)}. \tag{14}$$

It can be written in terms of probe densities by making appropriate substitutions of equation (9) into equation (13). The result is

$$N_{3S} = \frac{2I_L(b)}{2I_L(b) + 2I_L(\imath)} \frac{1}{\bar{A}(b)}.$$

This is valid for any shape of particle and bond (under the same conditions as S_V in general). Gurland (1958) derived a similar relation under the assumptions of uniform spheres and uniform plates.

Mean Intercept Length L_3

A measure of linear size of a phase Φ is given by the mean intercept length $L_3(\Phi)$. It is given by (Underwood 1970):

$$\bar{L}_3(\Phi) = 2\frac{L_L(\Phi)}{\bar{I}_L(\Phi)} \tag{15}$$

Because it is inversely proportional to equation (10) it is not a third independent parameter. In some instances it may be a more appropriate size measure than $S_{V\Phi}(\Phi)$. If both the numerator and denominator are measured simultaneously, with the same test system, a simpler form arises:

$$L_3(\Phi) = 2\frac{L(\Phi)}{\bar{I}(\Phi)}.$$

L_3 measures the average straight line traverse through phase Φ. In the case of a system of uniformly sized spheres, of diameter d, this implies that $L_3 = \frac{2}{3}d$ (Fullman 1953). One additional relation that can sometimes be of use, is obtained by combining equations (10) and (15). When this is done a relationship between the mean intercept length, mean volume, and mean surface area, of phase Φ, is obtained, and is given by

$$L_3(\Phi) = \frac{4\bar{V}(\Phi)}{\bar{S}(\Phi)}.$$

It is occasionally of interest to know the mean free path of particles within the pore space of a material. In a saturated two-phase material of pores (π) and grains (g) ($L_L(g) + L_L(\pi) = 1$), there is a simple relation between mean free path and the mean grain intercept length. Letting λ_π denote the mean free particle path (mean pore intercept length), it is given by (Dehoff and Rhines 1953):

$$\lambda_\pi = 2\frac{L_L(\pi)}{I_L(\pi)} = 2\frac{1 - L_L(g)}{I_L(g)} = 4S_V^{-1}(g) - L_3(g). \qquad (16)$$

2.3 Volume Weighted Mean Particle Volume $\bar{v}_V$

An additional measure of particle size, $\bar{v}_V$, the *volume weighted mean particle volume*, can be estimated from a single surface section. No assumptions regarding specific particle shapes are needed. This is particularly useful when particles have shapes not easily described by standard geometries. In snow studies, where preparing surface sections is extremely time consuming, making serial sections is often impractical. In those cases $\bar{v}_V$ provides the only general expression of particle volume which can be determined from a single surface section. An additional advantage is that the second moment, $\overline{v_V^2}$, can also be estimated from the same surface section.

Volume is an important parameter when examining grain growth, since grain growth implies an addition or subtraction of mass. It is the amount of material that characterizes a grain's size. This is even more important when grains are not spherical, in which case radius may not be the most suitable parameter for characterizing average size. Although, $\bar{v}_V$ is related to the average particle volume $\bar{V}$, they are not equal unless all particles have the same volume. In measuring average volume, each particle's volume $v(Y_i)$ is weighted in proportion to its volume fraction, where $w_i = v(Y_i)/\sum v(Y_i)$ in equation (3). It follows that $\bar{v}_V$ is given by

$$\bar{v}_V = \sum_i v(Y_i) \frac{v(Y_i)}{\sum_j v(Y_j)}.$$

This is the same measurement that would be obtained by sieving, where each sieve class is

weighted by the volume fraction or weight fraction of that class.

The relationship between volume weighted mean volume and number weighted mean volume is (Gunderson and Jensen 1985)

$$\bar{v}_V = \frac{\overline{V^2}}{\bar{V}}.$$

Where $\bar{V}$ and $\overline{V^2}$ are respectively the first and second moments of the volume weighted in number (equation (4) with weight $w_i = 1/n$, n being the number of particles measured). Gundersen and Jensen (1985) point out that, when the coefficient of variation $CV(V) \leq 0.25$, then $\bar{V} \leq \bar{v}_V \leq 1.06\bar{V}$. The significance of this is that even if $\overline{v_V}$ is a biased estimate of $\bar{V}$, that bias may be quite small and therefore negligible.

Gundersen and Jensen (1985) developed a two step procedure which allows estimation of $\bar{v}_V$ from a single surface section. In step one, sampling is performed using a point grid. This amounts to sampling in proportion to particle volume, since the probability of a point from the grid intersecting a particle is proportional to that particle's volume. Each particle intersected by a point of the grid is measured in step two.

Each sampled particle is measured in terms of the lengths of the intercepts generated by passing a randomly oriented line through the particle profile and sampling point. That is, for each grid point lying in a particle profile, x_j, an isotropic test line is passed through that point (see Figure 2). From this probe several lengths are recorded, all relative to the sampling point. The primary intercept length, L_{0j}, is the uninterrupted length of probe line through x_j. Interrupted line probe lengths are also measured. They are denoted by $L^e{}_{ij}$, the

ith particle profile entry, and L^x_{ij} the ith exit of the particle profile. See Figure 2 for an illustration. The particle sampled at sample point x_j has a volume weighted volume v_{Vj}, where (Gunderson and Jensen 1985)

$$v_{Vj} = \frac{\pi}{3}\left((L_{0j})^3 + 2\sum_{i}^{k}((L^x_{ij})^3 - (L^e_{ij})^3)\right) \tag{17}$$

and k is the number of extra intercepts (intercepts not containing the sampling point). If m is the number of sampled points, then volume weighted mean volume is

$$\overline{v_V} = \frac{1}{m}\sum_{j=1}^{m} v_{Vj}. \tag{18}$$

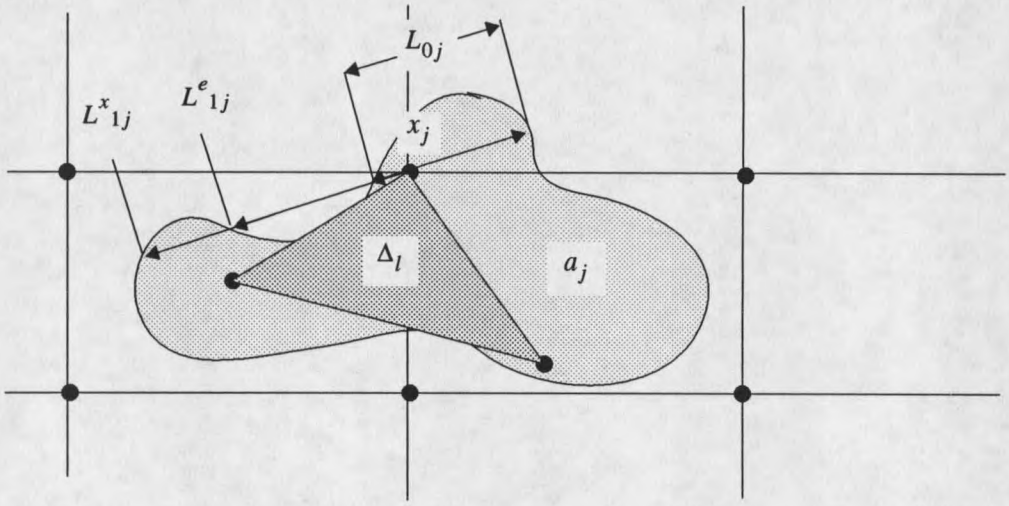

Figure 2. A point sampled particle and intercepts generated by a random test line through the test point.

Estimating the second moment is a bit more involved. For each sampled point x_j two additional points, contained in the particle's profile, are needed. These points, selected at random, and x_j form a random triangle of area Δ_j. If a_j is the total profile area of the particle with sample point x_j, then the second moment of volume weighted volume, $\overline{v_V^2}$, has as an unbiased estimate (Gundersen and Jensen 1985)

$$\overline{v_V^2} = 4\pi\overline{(a^2\Delta)} = \frac{1}{m}\sum_{j=1}^{m} a_j^2\Delta_j. \tag{19}$$

See Figure 2 for an illustration. To generate additional random points, a Monte Carlo type numerical scheme is used.

In particle aggregates it is known that particle volumes often follow a lognormal distribution (Miles 1985). In such a case the following simple relation exists between $\bar{v}_V$, $\overline{v_V^2}$, $\bar{V}$ (Miles 1985):

$$\bar{V} = \frac{(\overline{v_V})^3}{\overline{v_V^2}}. \tag{20}$$

Once the mean volume is available, several other parameters values may be estimated.

Some of the more useful relations are the mean number of particles per unit specimen volume,

$$\overline{N_V} = \frac{\bar{A}_A}{\bar{V}},$$

mean particle caliper diameter

$$\overline{M_1^{(3)}} = \frac{\bar{V}}{\bar{a}},$$

and the mean particle free surface area

$$\bar{S} = \frac{\bar{V}}{V_V} \overline{S_V}.$$

N_V and $\bar{S}$ are self explanatory. The mean particle caliper diameter $\overline{M_1^{(3)}}$ measures, for an arbitrarily shaped single particle, the average maximum normal distance between two parallel planes, when averaged over all possible particle orientations, each tangent to the particle surface.

Even if the particles don't follow a lognormal distribution, $\bar{v}_V$ may, by itself, provide an acceptable estimate of $\bar{V}$. If so the estimates just presented still hold, though, they may be slightly biased.

2.4 Circular Disks

In Chapters 4 and 5 much of the focus will be on grain bonds. There it will be assumed that to a reasonable approximation, grain bonds are circular disks. Two related parameters can be estimated, mean disk radius and mean disk area. A discussion of their roles as microstructural parameters is given in Chapter 4.

The expression for mean disk radius is valid for any distribution of circular disk radii. An expanded view, showing the intersection of a disk by a section plane, is shown in Figure 3. The disk has radius R_i and profile length $d_i = 1/m_i$. Mean disk radius is given by

the expression (Fullman 1953)

$$\bar{R} = \frac{\pi}{4\bar{m}_d}, \tag{21}$$

where $\bar{m}_d$, the harmonic mean of N intercept lengths, is

$$\bar{m}_d = \frac{1}{N}\sum_{i=1}^{N}\frac{1}{d_i}. \tag{22}$$

Fullman also developed an expression for mean surface area, $\overline{S_d}$, where

$$\overline{S_d} = \frac{\pi^2\bar{a}}{2\overline{m_d}\bar{l}} = \frac{\pi^2 N_L(d)}{2\overline{m_d}N_A(d)}. \tag{23}$$

$\bar{a}$ is the average disk cross sectional area, $\bar{l}$ is the average intercept length of the intersected disks, $N_L(d)$ is the number of disk profiles intersected per unit length of test line, and $N_A(d)$ is the number of bond profiles per unit probe area.

From the middle expression of equation (23) a different stereology relation results if the disk thickness is negligible. This assumption is made in Chapters 4 and 5. Letting the disk profile thickness be δ, a constant, the average disk cross sectional area can then be written as $\bar{a} = \delta\bar{d}$ and the mean disk intercept length as $\bar{l} = \delta$. Substituting these into the middle expression of equation (23) and multiplying by 1/2 gives the following expression for mean disk area:

$$\overline{A_d} = \frac{\pi^2\bar{d}}{4\overline{m_d}}. \tag{24}$$

Note that by including a factor of 1/2 only the disk area is measured not it its total surface area.

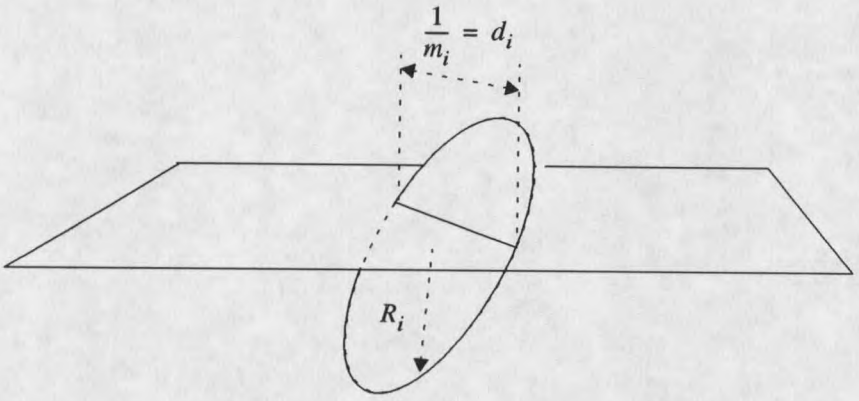

Figure 3. This shows the relationships between a randomly oriented disk of radius R_i, which has been intersected by a sectioning plane. The intersection of the plane and the disk is a straight line of length $d_i = 1/m_i$.

2.5 Edge Effects and Guard-Zones

There is one aspect of probe measurements that is yet to be discussed. Plane sections are quite often too large to be sampled in their entirety. Sub-regions or quadrats are used instead. The boundary of a quadrat, placed at random on a section, will almost surely intersect one or more profiles (see Figure 4). How are those objects intersected by the quadrat to be handled during probe measurements? As would be expected, those lying wholly within the quadrat are treated as complete profiles. Because full knowledge of those object profiles intersected by the quadrat boundary are not available, special care must be given to them in order to minimize measurement errors and bias. This situation is generally referred to as the edge effect. Referring to Figure 4 it is not clear how to, for example, count the number of objects per unit area, nor is it obvious how one might mea-

sure the uninterrupted object traverse lengths of those objects intersected by the quadrat boundary. One way of dealing with the edge effect is through the use of guard-zones and associated points (Miles 1978; Jensen and Sundberg 1986).

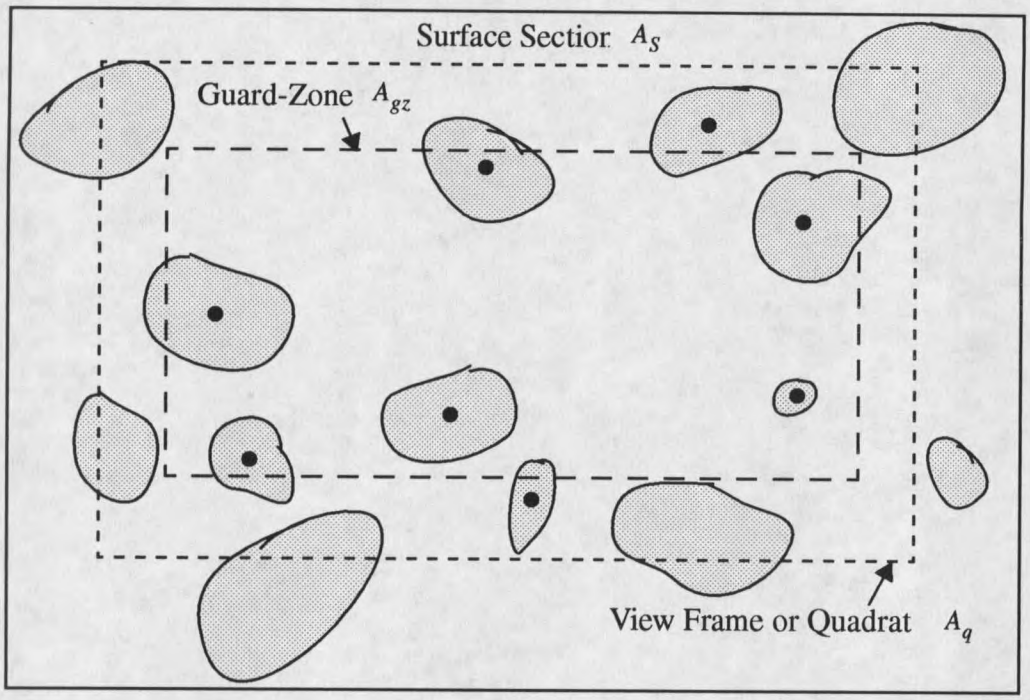

Figure 4. Example of a surface section A_S, view frame or quadrat A_q, and a guard-zone A_{gz}. A_{gz} is the largest rectangular region that does not intersect any object not wholly contained within A_q. For each object in the figure, there is only a single associated point (black dots) per object. Only those objects which have an associated point lying within an associated point analysis area A_{ap} are considered in any associated analysis. In the figure $A_{ap} = A_{gz}$.

The guard-zone A_{gz} is a very simple idea. It is a bounded region contained within a quadrat such that no object profile is intersected by its boundary if that profile is also intersected by the quadrat boundary. This is illustrated in Figure 4. It should have a fixed shape, for example a rectangle. The guard-zone will be used when measuring the volume

weighted mean volume (Karlsson and Cruz-Orive 1991), where the sampling points are constrained to lay within the guard-zone. Because the guard-zone intersects only profiles that are contained within the quadrat, traverse measurements will be made only on complete object profiles.

In the associated point method, using some predefined criteria, one or more associated points are assigned to each profile. There are many ways of making such assignments. For example, the centroid of a planar profile or end points of a line segment. Assignments must be consistent for each object profile under consideration. Although it is possible to assign associated points to a profile which is intersected by the quadrat A_q (Jensen and Sundberg 1986), only associated points for profiles contained within A_q will be considered here. The general idea is illustrated in Figure 4 where the black dots are associated points. Once the associated points have been assigned, an analysis region A_{ap} contained within the quadrat is selected. It can be a randomly placed region or a guard-zone such as that described earlier.

Profile counts weighted inversely proportional to the number m of associated points per object, i.e. $w_i = 1/m$. While one and two dimensional profile measurements are weighted in proportion to the number of associated points, k_i, each profile has within A_{ap} and inversely proportional to the number of associated points per profile, i.e. $w_i = k_i/m$. As an example, let A_{ap} be given by the guard-zone shown in Figure 4, that is $A_{ap} = A_{gz}$. Then, with the associated points shown and with $m = 1$, the number of profiles per unit area $N_{A\alpha}$, is given by:

$$N_{A\alpha} = \frac{N(\alpha_1)/1}{A_{gz}},$$

where $N(\alpha_1)$ is the number of associated points contained within A_{gz}.

In Chapter 5, disk (bond) profile's are measured only if their profile center is contained within a specified associated point area A_{ap}. A similar approach is used for neck measurement, more about which will be said in Chapter 5. The selection of A_{ap} is described when needed in Chapter 5.

CHAPTER 3

DIGITAL SKELETONIZATION

As noted in the last chapter, particle measurement can be conducted only if particle section profiles are distinct and identifiable. Applying a particle description to materials such as consolidated snow and then attempting to make related measurements is troublesome. The phase descriptions which are of interest do not yield easily identifiable profiles. Bond and neck profiles must, in fact, be inferred from those profile geometries which are visible. Upon inferring one of these phase's profiles, the section can be partitioned, lines drawn, and regions shaded accordingly. Application of stereology probes can then be carried out assuming that the partitioned section holds the correct profile information.

We can see then that particle-based analysis of consolidated snow requires a set of criteria which identify characteristic phase profile markers in terms of visible profile geometries. Given those, it is essential that they be applied as objectively and consistently as possible. Since images of surface sections can be stored digitally, implementing identification and partitioning procedures in the form of computer software suggests itself. As the identification criteria will be geometrically-based, software automation must be capable of analyzing profile geometry. In this chapter a method, *skeletonization*, is reviewed.

It can be implemented in software and can be used to perform the necessary profile shape analysis. Identification criteria will be discussed in the next chapter.

As we will see later, skeletonization, generates a lineal representation of an area profile. The profiles contain all of the topological information needed to effect shape analysis for bond, neck and grain phase identification criteria which are developed in the next chapter. Shape skeletons turn out to be ideal for implementing software-based area shape analysis.

There are a number of skeletonization techniques documented in the literature, each having its own advantages and disadvantages. The one presented here (Meyer 1988) was chosen because of the properties of the skeletons produced and because it is a fixed step algorithm. Meyer's (1988) skeletonization algorithm focused primarily on hexagonal digital domains (pixels are arranged in a hexagonal pattern). Either special video monitors and digitizers or image re-sampling (it produces a coarser image) are needed to properly implement that form of the algorithm.

Standard computer monitors have pixels arranged in square or rectangular arrays. This is also the standard format of scanners and digital cameras. The purpose of this chapter is to show how Meyer's algorithm is implemented when the digital domain is square (section 3.3). It is presented in terms of specific neighborhood configurations and connectivity criteria. Step one of his three-step procedure is a direct translation. For step 2, Meyer (1988) gave a set of quite general rules which are valid for a wide range of digital domains. As stated later, these rules will reflect a square domain and enough specificity to produce thinner skeletons than can be obtained via his more general rule statement. Step three can be based upon his algorithm. Unfortunately, a number of difficulties were encountered. As a consequence a modified procedure, which accomplishes the desired results, is given instead.

In the sections 3.1 the definition of a skeleton is given. Some preliminary concepts and definitions regarding digital domains that are needed in section 3.3 are given in section 3.2. A short pictorial sequence is shown in the last section which illustrates the various steps that occur during image skeletonization.

3.1 Definition of the Skeleton

The definition of a skeleton is most easily stated for the real plane $\Re^2$. Given an open set X in $\Re^2$, and a point $x \in X$, let $R_X(x)$ be the largest disk contained in X with center x. The radius of $R_X(x)$ is the minimum distance from $x \in X$ to a point in the set X^C, the compliment of X. A point $y \in X$ is then said to be the center of a maximal open disk in X if for any $x \in X$, $x \neq y$, $R_X(y)$ is contained in X but not in any other disk $R_X(x)$. $S(X)$, the skeleton of X, is then defined to be the set of centers of maximal open disks contained in X (Matheron 1988).

In Figure 5 an ellipse, labeled X, is shown with two open disks. Even though the disk $R_X(u)$ centered at $u \in X$ is the largest centered at that point and also contained in X, it is not a maximal disk, since it is contained in a larger disk which is also contained in X. The disk $R_X(y)$ is maximal in X, since it is contained in no other disk also contained in X. The boundary of the open disk $R_X(y)$ and $R_X(u)$ each contain at least one point z of the boundary ∂X of X and so the closed disks are both tangent to ∂X at z.

The set of maximal disk centers, $S(X)$, are not necessarily connected, even if X is. In some instances (for example, a shape analysis tool described by Pirard (1994)) this is not a problem. To carry out identification and partitioning, as intended here, a path-connected skeleton is needed. The skeleton algorithm to be presented in section 3.3 does generate a path connected skeleton which is also homotopic to X (basically the skeleton has the same number of loops as there are holes in X and also has the same connectivity).

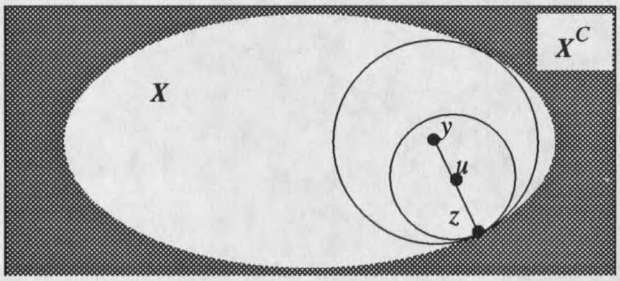

Figure 5. The disk centered at y is a maximal disk in X. The disk centered at u is not a maximal disk in X since it can be contained in larger disks also in X.

3.2 Digital Neighborhoods and Connectivity

Each point of a digital set has associated with it a specific neighborhood and connectivity criteria. An 8 neighbor neighborhood, illustrated in Figure 6, is the neighborhood chosen in this study. In that Figure, the central point u is shown with lines radiating toward each of its 8 neighbors, which are denoted by n_i, i=1,...,8. In a digitized image, these would be simply eight neighboring pixels contained in the profile. A neighbor of the central point u is called an 8 neighbor of u.Given $u = (x_0, y_0)$, $n_i = (x_i, y_i)$ is an 8 neighbor of

u if $|x_i - x_0| = 0$ or 1 and $|y_i - y_0| = 0$ or 1. The Euclidean distance $d_i(u, n_i)$ from u to n_i is either 1 (i odd) or $\sqrt{2}$ (i even).

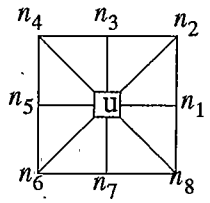

Figure 6. Neighborhood of a point u for a digital domain. Possible paths between neighbors shown by the solid lines.

The definition of *connectivity* used here is called 8-connected. This says that if two points, u and v, have values in a set C and if v is an 8 neighbor of u, then u and v are connected (Gonzalez and Woods 1992). To help clarify this concept consider the following example. Suppose C is a set of color values ranging from 10 to 15. Suppose that each point of a set U may have a color value between 0 and 255. Then, if u is a point, having a color value in C, and v is an 8 neighbor of u also having a color value in C, u and v are 8-connected. If v is an 8 neighbor of u but its color value is not in the set C then u and v are not connected. Two different notions of the set C are needed and will be defined as appropriate.

3.3 Skeletonization

In practice, digital images will contain several distinct area profiles. The skeletonization algorithm that follows, applies equally to a domain with one or several profiles, but

for simplicity, is described here in terms of a single profile. The containing space or image will be denoted by I_M. Contained in that space is a area profile X. It is the skeleton of X that is to be generated.

As mentioned earlier, the modified skeletonization algorithm to be described next is based upon one developed by Meyer (1988) for discrete hexagonal domains. That algorithm proceeds in three steps. In the first, a distance map, $D_M(X)$, of X is created. It gives the minimum distance from each point in X to the complement of X (points not in X). Step two extracts a set of points $C_P(X)$ in X, called crest points, from $D_M(X)$. These correspond roughly to centers of maximal disks in X. Since $C_P(X)$ might not be connected, step three determines the smallest set of points $C_C(X)$, from $D_M(X)$, such that $S_K(X) = C_P(X) \cup C_C(X)$ is connected. For the specific purpose for which skeletons will be used, considerable extraneous information is produced. In the last part of this section, details pertinent to simplifying the skeleton representation are described, namely *thinning* and *pruning*.

The Distance Map

Determining the skeleton of an area profile X begins by constructing its distance map $D_M(X)$. $D_M(X)$, which looks much like a Topographical contour map, gives the minimum distance from each point of X to the complement X^C (points not in X) of X. It is nothing more than a digital map of $\rho(x)$. Initially, each point in I_M is assigned one of two values, zero or L, where L is some large integer. L needs to be at least as large as the maximum

traverse distance across X. Assignment of zero and L proceeds by setting each point of X^C to zero and each point of X to L. To generate the distance map $D_M(X)$ Meyer (1988) used the Rosenfeld-Lay algorithm. Two passes over I_M are required. The first pass starts at the upper left of I_M (0,0). Scanning in direct video order (left to right and top to bottom) a new distance value $\bar{d}_x$ is assigned to each x of X. It is determined by

$$\bar{d}_x = min[d_x, \bar{d}_2 + d_2(x, n_2), \bar{d}_3 + d_3(x, n_3), \bar{d}_4 + d_4(x, n_4), \bar{d}_5 + d_5(x, n_5)]. \quad (25)$$

$\bar{d}_2, \bar{d}_3, \bar{d}_4$, and, $\bar{d}_5$ are distance values assigned to the corresponding points of X during the current pass. Note: on the first pass, d_x will read either 0 or L depending upon the initialization value assigned to that point. Also, when the current point x is at a border row or column, neighbors lying outside of I_M take over bar values of zero (both the first and second passes).

On the second pass I_M is scanned in reverse video order (right to left and bottom to top). It begins at the lower right hand corner (the last point scanned during the first pass). Each point x of X is now assigned a new distance value $\hat{d}_x$, given by

$$\hat{d}_x = min[\overline{d}_x, \hat{d}_6 + d_6(x, n_6), \hat{d}_7 + d_7(x, n_7), \hat{d}_8 + d_8(x, n_8), \hat{d}_1 + d_1(x, n_1)]. \quad (26)$$

As in the first pass, the over hat values, $\hat{d}_6, \hat{d}_7, \hat{d}_8$, and, $\hat{d}_1$, are distance values assigned to the corresponding points of X during the current pass. $\overline{d}_x$ is the distance value assigned (equation (25)) to x during the first pass. An example of a distance map is shown in the right half of Figure 7. It corresponds to the shape X on the left of that figure.

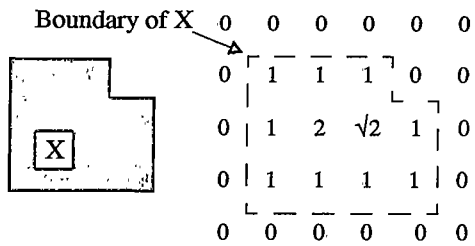

Figure 7. The set X is transformed by equations (25) and (26) into the distance map shown on the right. Points not in X all have distance values of zero.

Crest Points

With the distance map $D_M(X)$ completed the Crest Points $C_P(X)$ can be found. Below, is a version of Meyer's (1988) general definition, stated specifically for an 8-neighbor neighborhood and 8-connected connectivity criteria.

Analysis of each point x in X, begins by making a temporary assignment of zero's and one's to x and each of its 8-neighbors (Meyer 1988). Recall that each point u in $D_M(X)$, has been assigned a value corresponding to the minimum distance $\rho_s(u)$ from itself to the boundary of X. $\rho_s(u)$ is the discrete form (square domain) of $\rho(u)$. With that, assignments are made as follows. If v is an 8-neighbor of u for which $\rho_s(u) < \rho_s(v)$, then v is assigned the value 1. If v is an 8 neighbor of u such that $\rho_s(v) < \rho_s(u)$, v is assigned the value zero. Finally a collection $\{N_i\}$, of neighborhoods, is formed by assigning all possible combinations of zero and one to the remaining neighbors z of u for which $\rho_s(z) = \rho_s(u)$.

With those assignments made, u is a *crest point* if any of the following value assignments, for any of the $\{N_i\}$, hold:

C1) assigning u the value 1 makes it the only point of its 8-neighbor neighborhood with a value of 1,

C2) assigning the value 0 to u creates a connected path between two of its neighbors having zero values 0, that, would not otherwise be connected in the neighborhood of u,

C3) assigning a value of 1 to u creates a connected path between two of its neighbors that, would not be otherwise connected in the neighborhood of u.

There are three classes of neighborhoods appearing in $\{N_i\}$. Up to rotations, they have the forms shown to the left of each arrow of Figure 8. The first crest point criterion, C1 is satisfied upon assigning one to the central point. Similar central point assignments to configurations in $\{N_i\}$ which lead to the central point satisfying either C2, (b) of the figure, or C3, (c) of the figure. Other possible configurations, corresponding to (b) and (c) of Figure 8, follow after rotations of $\pi/4$.

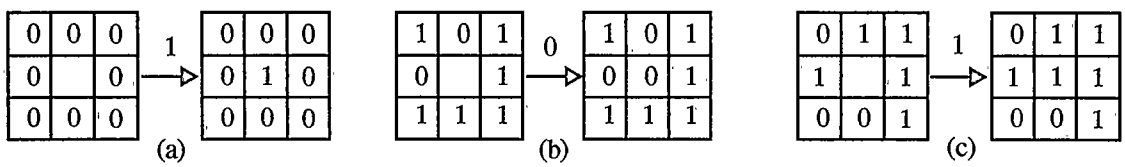

Figure 8. Each neighborhood shown without a central value was formed using the coding scheme described in the text. (a) Assignment of 1 to the central point creates a neighborhood satisfying criteria 1. (b) Assignment of the value 0 to the central point creates a neighborhood satisfying criteria 2. 1 could be assigned and then criteria 3 would be satisfied. (c) By assigning 1 to the central point criteria 3 is satisfied. A 0 could be assigned so that criteria 2 is satisfied. Notice in (b) for example that the two neighbors with values of 0 are not connected unless 0 is assigned to the central point.

Connection Points

Since the goal is the generation of a connected skeleton for X, in the last step a set of points $C_C(X)$ is formed such that $C_P(X) \cup C_C(X)$ is connected (8-connected sense). Connectivity now means that, two points x and y, both in $C_P(X) \cup C_C(X)$, are connected if y is an 8 neighbor of x where $\rho_s(x) > 0$, $\rho_s(y) > 0$. At this step, Meyer (1988) used a three pass algorithm to generate a set of points called the Upstream. Due to problems in guaranteeing connectivity on a square domain when using his algorithm, a different approach has been opted for. The final result is essentially the same, but implementation is far simpler.

Let $\Sigma_i(X) = C_P(X) \cup C_{Ci}(X)$ denote the union of crest points and i connections points. $D_M(X)$ is scanned in sequential order until a point y also in $\Sigma_i(X)$ is found. From y the steepest uphill path is traversed until either any point z in $\Sigma_i(X)$ is reached, or a point w is reached from which no uphill step is possible. Each point of the path joining y and z or w is added to $C_{Ci}(X)$. If the terminating point is w it is also added to $C_{Ci}(X)$. Upon reaching the lower left of $D_M(X)$ the augmented skeleton $\Sigma_A(X)$ of X is complete.

Thinning and Partial Pruning

The augmented skeleton $\Sigma_A(X)$ actually contains more information that is needed for bond, grain, and neck identification. Robust analysis of a skeleton is best achieved if it is reduced, as far as possible, to a one pixel thickness. What are referred to as dendrites

(Meyer 1988), generally do not contain shape information critical to successful identification. Where possible, these can be removed and is termed partial pruning.

The reduced skeleton, $\Sigma(X)$, obtained by thinning and partial pruning of $\Sigma_A(X)$, should preserve homotopy. That means that $\Sigma(X)$ has the same connectivity and the same number of holes as X.

Due to the discrete domain on which the skeleton is constructed, occasionally artificial one-pixel holes are created. Because it is difficult to determine whether or not these single pixel holes are actually part of X and since they are, more often than not, all single pixel holes are filled.

To guarantee that $\Sigma(X)$ is a single connected set, no pixel can be removed from $\Sigma_A(X)$,by thinning or partial pruning if the resulting set becomes disconnected as a result of the removal. The last requirement to be satisfied by thinning and pruning is that $\Sigma(X)$ and $\Sigma_A(X)$ have the same maxima and non end-point minima. Local minima situated at dendrite end-points can be removed since they play no identification role.

Thinning criteria can be stated as follows. If a point x in $\Sigma_A(X)$ is to be removed,

T1) removal of x must not change the homotopy of $\Sigma_A(X)$

and

T2) when x is not a dendrite end-point, there is at least one 8-neighbor y of x such that $\rho_s(x) < \rho_s(y)$ holds.

Partial Pruning criteria allow removal of a point x in $\Sigma_A(X)$ if it is an end-point such that

P1) T1 and T2 are satisfied

and

P2) for each 8 neighbor y of x, $\rho_s(x) < \rho_s(y)$, when ever y is in $\Sigma_A(X)$.

See Figure 9 for an illustration of these criteria. Shown is a central point x where $\rho_s(x) = 1$ and where its only 8-neighbor y in $\Sigma_A(X)$ as a distance value $\rho_s(y) = 2$. P1 and P2 are both satisfied and so x can be removed. Note, if, in the figure, it were the case that $\rho_s(x) = 2$ and $\rho_s(y) = 1$, x could not be removed since P2 would not be satisfied.

0 0 0
0 1 2
0 0 0

Figure 9. A skeleton end point configuration. 1 is the end point. 1 and 2 correspond to points in $\Sigma_A(X)$.

A detailed analysis of particle shape would likely require that no partial pruning be performed. Thinning may still be required, since, most of the points which add thickness to a skeleton provide no essential shape information.

3.4 A Pictorial Example

The following set of images demonstrate the skeletonization of surface sections. Figure 10 shows a small portion of a surface section that was obtained from a larger gray

scale image. After filtering, enhancement, and thresholding, a binary (black and white) representation of (Figure 11) is obtained. Ice-grains are black and the pore space is white.

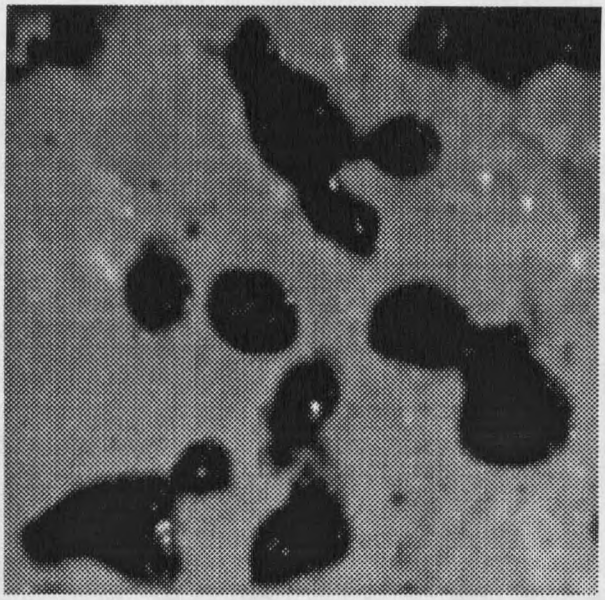

Figure 10. Part of a surface section.

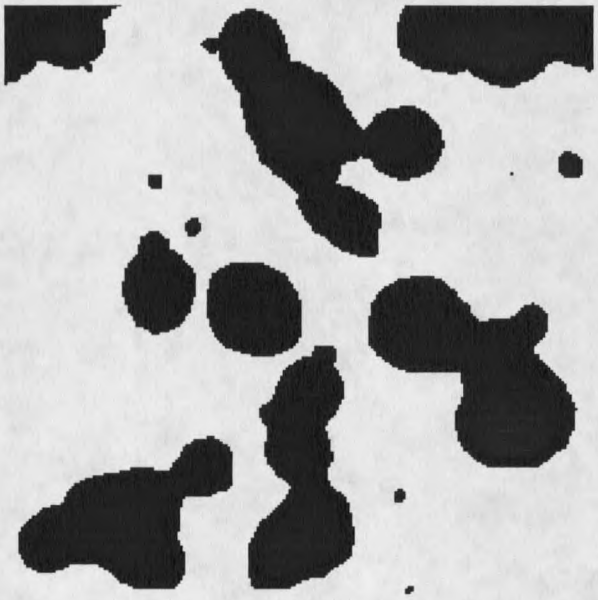

Figure 11. The binary representation of Figure 10.

When the distance map algorithm is applied to Figure 11 the result is the new representation shown in Figure 12. In that figure, equal distances from the boundary, correspond to equal gray levels. The next transformation is accomplished by applying the crest point criteria to the distance map. The set of points that is generated from Figure 12 yields the non-connected skeletons illustrated in Figure 13. They are shown superimposed upon the original binary image.

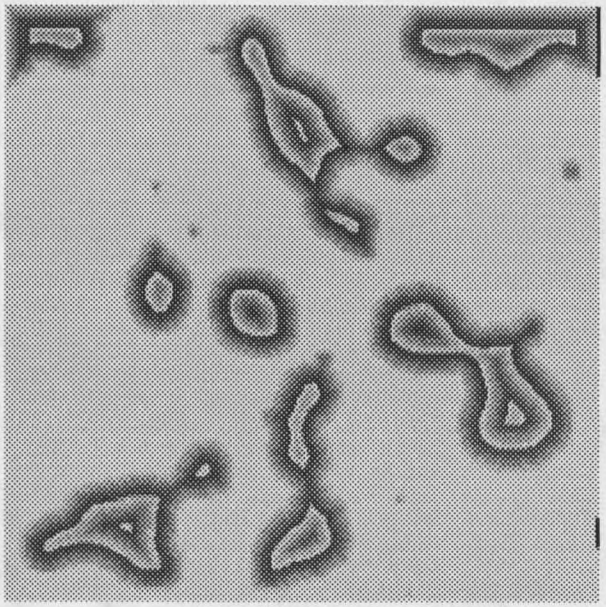

Figure 12. The distance map corresponding to grains (black) of Figure 11.

In order to connect the crest points, the distance map and the set of crest points are scanned simultaneously in order to determine those points that are in the set of connection points. When this is done, using Figure 12 and Figure 13, the set of connected skeletons shown in Figure 14 are the result.

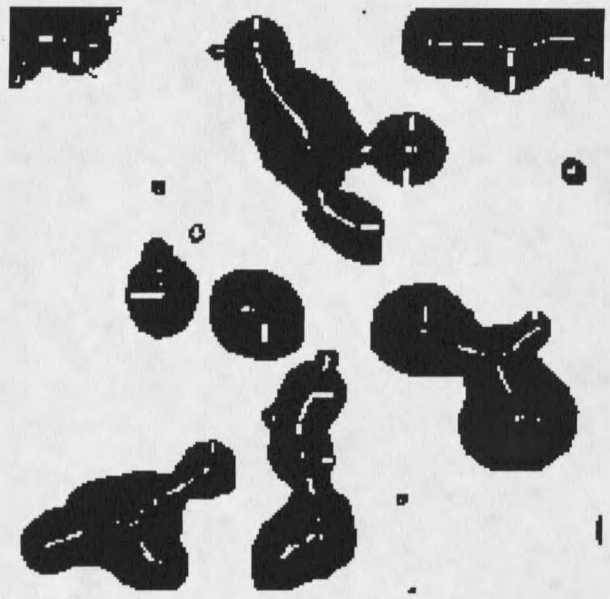

Figure 13. The crest points corresponding to the distance map of Figure 12. Note how disconnected these are.

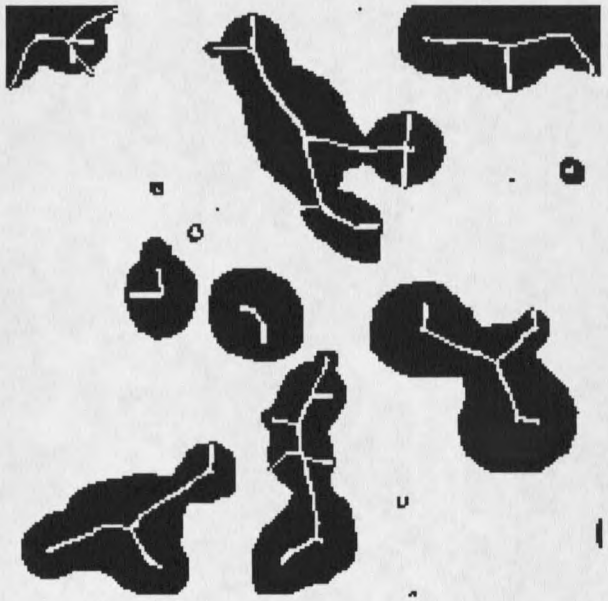

Figure 14. The connected skeletons for the grains of Figure 11. Each skeleton is the union of a set of crest points, illustrated in Figure 13, and the additional set of points needed to connect that skeleton's crest points.

The last transformation step is to thin and partially prune the skeletons of Figure 14. As shown in Figure 15 the resulting skeletons are much simpler in form as well as being much thinner. Even though the amount of skeleton information, describing each grain, has been reduced, that information which is crucial for bond and neck identification (Chapter 4) is still present.

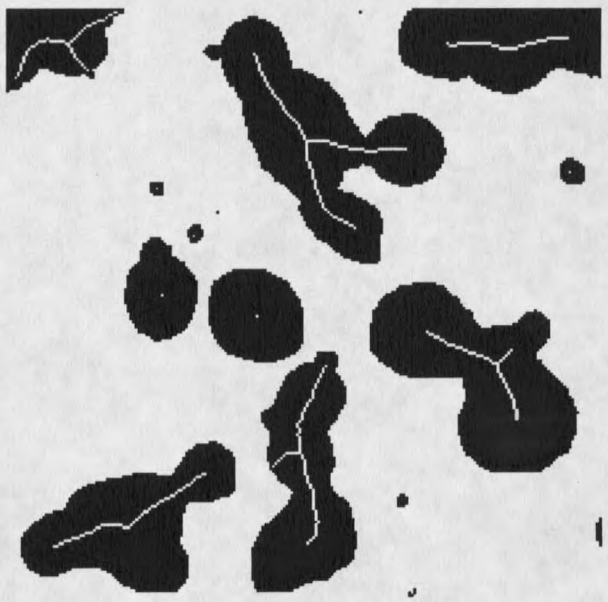

Figure 15. A thinned and partially pruned version of the skeletons shown in Figure 14.

CHAPTER 4

MODELING AND MEASUREMENT OF BONDS AND NECKS

A volume of consolidated snow has two major constituents, ice and air. These produce snow's internal structure by combining in the form of ice-grains and pores. The ice exists as an interconnected network and is the load bearing part of the snow. Surrounding it is a complementary structure, the pore space. The pore space is a fluid medium, typically air, vapor, and or water. It may consist of both isolated and interconnected parts. Consolidated snow occurs when an aggregate of discrete ice particles come into contact, at which point sintering processes create solid inter-grain connections at those contacts. Most physical properties and characteristics of consolidated snow may be directly attributed to its particular internal structure.

Parameter representations of internal structure are often found in physical models. They may characterize some aspect of either the ice matrix, pore space, or both. These characterizations typically rely on a component based constituent description. For example the ice matrix may be treated as composition of discrete structural components such as ice-grains and grain-bonds (inter-grain connections). Other ice matrix representations are possible (one of which, the neck, is discussed later). The pore space can be treated in a similar manner.

Component parameters may include volume, area, size, and number density. Normally these parameters represent an average characteristic, although, distributions may also be used. There are a number of ways to measure these and other parameters. Some of the more common methods are dis-aggregation and sieving, thin sections and opaque surface sections, the latter two being used in conjunction with quantitative stereology. All of these are destructive techniques. Surface sections are the primary method of interest here. Surface sections yield two dimensional cross section views of a material's internal structure. Visible on a cross section will be spatially distributed discrete ice- and pore- profiles. Recall from Chapter 2 that a profile is the geometric shape produced by intersecting a material phase with a sampling probe.

In order to make measurements which reflect the underlying granular structure of consolidated snow, component section profiles must be in place at the time of measurement. Their superposition-based spatial distribution must be reconciled with any existing distribution of discrete ice- and pore- profiles, i.e. component profiles must be inferred from existing profiles. How such inferences are made will be directly reflected in the validity and accuracy of parameter values that result. Set rules, relating key profile features to counterpart component cross sections, are helpful. Such rules have been formulated for bond profiles by Kry (1975a) and Gubler (1978b) (both discussed in detail later). As pointed out by Dozier et al. (1987) these rules suffer from the lack of an available objective application method.

In this chapter, bond and neck profile rules are stated in terms of profile skeletons. This ties the identification criteria directly to an automation method. The result is a consistent and objective rule application. Brief descriptions of three-dimensional grain, bond, and

neck components are given first. Before reviewing Kry and Gubler's bond identification procedures and stating precise criteria, several relations between a profile boundary and its skeleton need to be derived. These relate maximal-disk boundary contact-points and boundary curvature to the skeleton and will then be used to formulate new criteria. Additional criteria for neck profile identification are then stated. Following that, stereology-based measurement of bonds and necks will be discussed. For bonds a brief review of Kry's (1975a) approach is given. For average neck length, a new relation is derived, providing upper and lower bounds.

4.1 Grain, Bond, and Neck Components of Consolidated Snow

Kry (1975a) defined a grain-bond as that plane surface of minimum cross section separating two grains. Brown (1979) defined grains as those structural elements which have predominately convex free surfaces (with respect to the ice interior). A neck was then defined as the ice region with predominantly concave free surface connecting two grains, and a bond as the minimum area cross-section of a neck. An example illustrating these definitions is shown in Figure 16.

It should be noted that the geometry represented here is somewhat unrealistic but is used to provide a clear demonstration of the make-up of the grain/neck structure. Normally necks are much shorter than shown here, since grains must invariably come into contact in order for a neck to form.

An alternative definition of grain-bonds can be devised which is independent of surface geometry. Dozier et al (1987) defined a grain-bond as the plane contact area formed

by two ice grains having different crystal orientations. This definition and Kry's definition are often coincident, but, not necessarily equivalent (Dozier et al 1987).

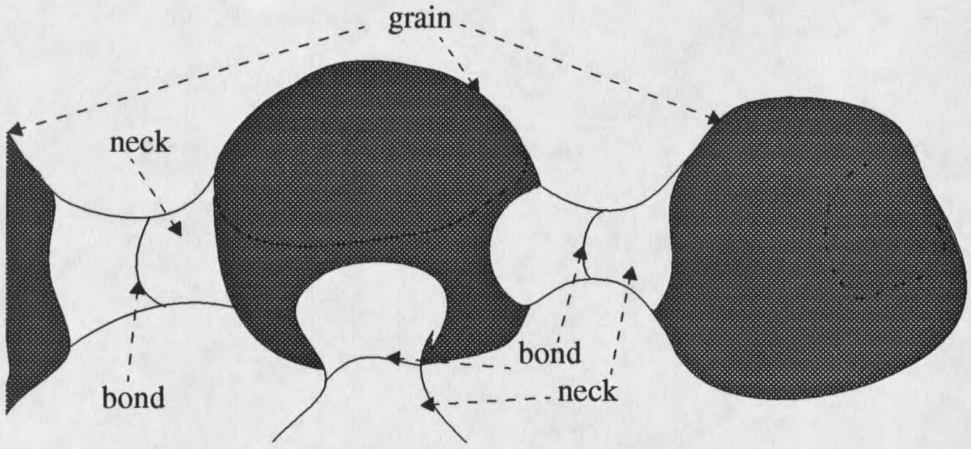

Figure 16. Part of an ice network showing grains, bonds, and necks.

It will be helpful later if some notation is established for the definitions just given. Consider two ice grains g_1 and g_2. If they are brought into contact and then adhere through a sintering process, a new ice surface S will be formed between them (see illustration in Figure 17). Let S_{R1} be the largest sphere which can be contained by grain g_1. Similarly let S_{Rj} be the corresponding sphere for grain g_2. Let S_R be a variable radius sphere with an initial radius equal to the smaller of S_{R1} and S_{R2}. For example let $S_R = S_{R1}$. Suppose that S_R is translated so that its center traces out a minimum length continuous path, c_{12}, from the center of S_{R1} to the center of S_{R2}, in such a way that S_R is always contained within the ice. Suppose further that the radius of S_R is always the maximum possible, consistent with the constraints of the previous sentence. Finally suppose that at a point c of

c_{12}, the radius $R(c)$ of S_R is an absolute minimum for the path interval defined by c_{12}. $S_R(c)$ defines the minimum constriction between the two mutually sintered ice grains g_1 and g_2. Define curve C_b to be that closed curve formed by the intersection of surface S and a plane passing through c, oriented perpendicular to c_{12} at c. The bond between grains g_1 and g_2 is defined as the plane b_P enclosed by the plane curve C_b (illustrated in Figure 17).

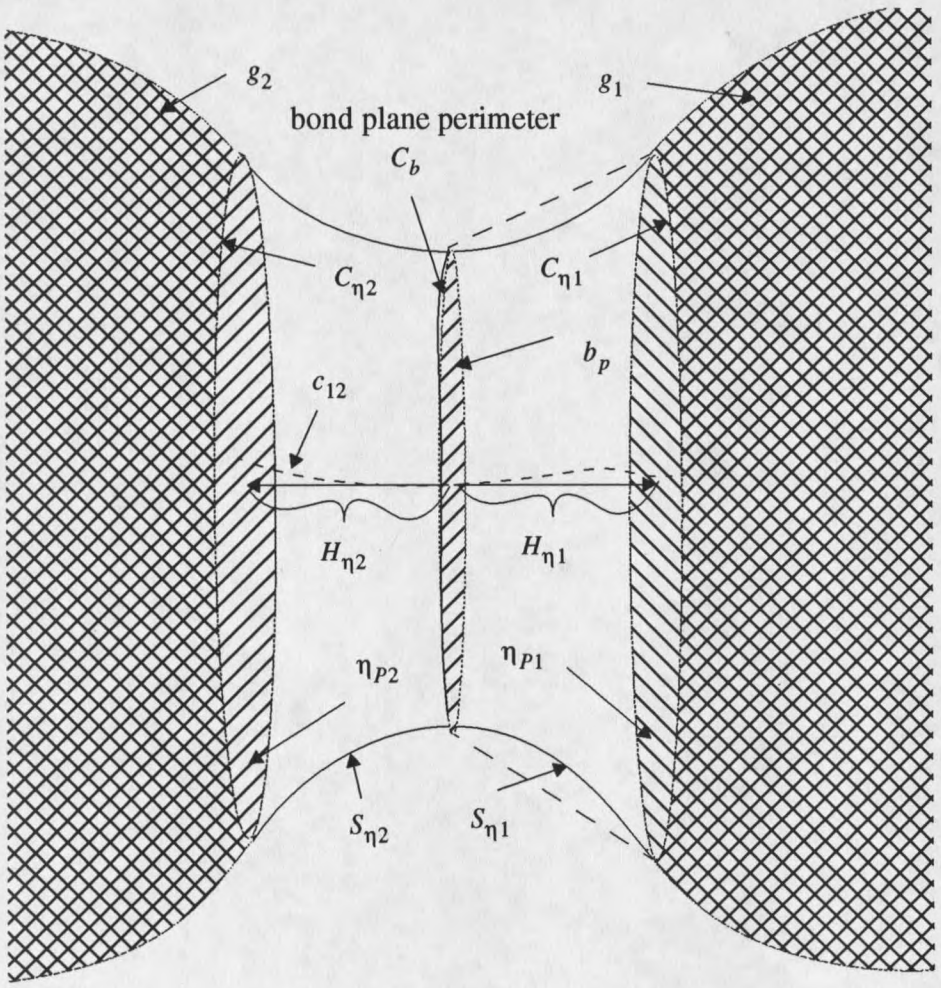

Figure 17. Grains g_1 and g_2 along with neck η_P connecting them.

In the transition from the grain surface (proper) to the bond perimeter, a change in sign of the curvature will be encountered. For simplicity it is assumed that all such points form a single continuous closed curve C_η which makes a complete traverse about the line c_{12}, defined earlier. Further simplification results if it is assumed that those points on the curve are co-planar, such as shown for the two curves $C_{\eta 1}$ and $C_{\eta 2}$ of Figure 17. The plane bounded by C_η defines the *neck base plane* η_P. Illustrated in Figure 17 are the two base planes η_{P1} and η_{P2}. The straight line from bond plane center to neck base plane center H_η defines what will be called the *half neck length.* Two half neck lines are illustrated in Figure 17, $H_{\eta 1}$ and $H_{\eta 2}$.

4.2 Profiles and Skeletons

Before stating precise bond and neck profile identification criteria, expressions relating a position w on a profile boundary, curvature at w, and a point s of the profile skeleton are needed. Definitions and other basic facts concerning skeletons and skeletonization of digital images have been reviewed in Chapter 3.

Skeletons and Profile Shape

Formally, in $\Re^2$, maximal disks are open sets contained in an area A_k and the generated skeleton, Σ_k, is defined by developing a one-to-one correspondence between Σ_k and the interior of A_k. The closure of Σ_k has the same connectivity as A_k (Matheron 1986). It

will be assumed that A_k has a closed boundary ∂A_k. From the definitions of a maximal disk it follows that the boundary of each open maximal disk in A_k has two or more points in common with ∂A_k (Matheron 1986). At those common points, both boundaries share the same tangent. In what follows, maximal disk will be used to denote the union of an open maximal disk and its boundary, and Σ_k will denote the union of the set of centers of open maximal disks in A_k and the smallest set of additional points needed so that Σ_k is a connected set. This corresponds the digital skeleton reviewed in Chapter 3.

In Figure 18 a planar shape is shown, along with its skeleton, Σ_k. It is the line segment $[s_1, s_2]$. Two different ways of looking at the relationship between the area's boundary and its skeleton, Σ_k, are depicted. Along interval $[s_1, s_0]$ several maximal disks, along with line segments emanating from their centers to points common to each maximal disk and to the profile boundary, are shown. These line segments are normal to the profile boundary and emanate from the skeleton at various angles. On the interval $[s_0, s_2]$ a functional representation of maximal disk radius versus position is shown. The maximal disk radius, at s of

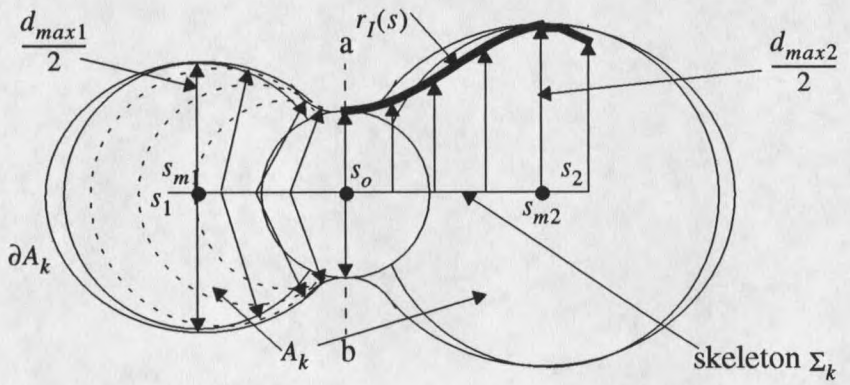

Figure 18. A cross section through a bonded grain pair showing the boundary profile and bond line location.

the skeleton segment $I = [s_0, s_2]$, is given by $r_I(s)$. In the next part, two important relationships are derived which depend upon $r_I(s)$.

Skeletons and Boundary Curvature

In this part ∂A_k is assumed to be a positively oriented closed curve (counter clockwise). A connected open segment B in ∂A_k is selected. To each point w in B is associated a closed disk with center s in a connected open segment S_B of the skeleton Σ_k. w is a parameter measuring distance along B from some origin w_0 and s is a parameter giving distance along S_B from an origin s_0. Therefore the terms s and w, while denoting specific points in Figure 19, are also used to denote coordinate positions along the curvilinear coordinates (curves) Σ_k and ∂A_k, respectively. The distance between s and w is just the maximal disk radius $r_B(s)$. It is assumed that r_B is a twice continuously differentiable function.

At each point w of B where a tangent is defined, the normal will be coincident with a line segment through w and s. If $\hat{n}_B$ is taken as the inward unit normal to B at w, then the vector r_{sw} from s to w can be written as

$$r_{sw} = -r_B \hat{n}_B. \tag{27}$$

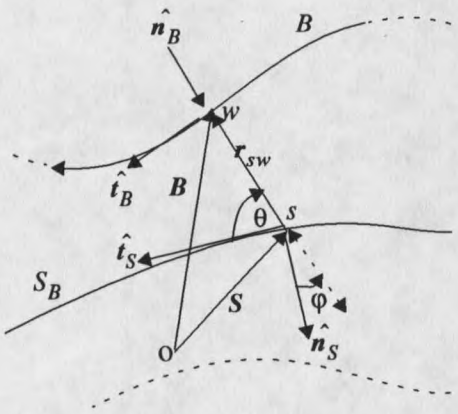

Figure 19. Geometry of boundary and skeleton.

Let $\boldsymbol{B}$ and $\boldsymbol{S}$ be position vectors from some common arbitrary origin o to s in S_B and w in B, respectively. It then follows from Figure 19 that r_{sw} also satisfies the relation

$$\boldsymbol{r}_{sw} = \boldsymbol{B} - \boldsymbol{S}. \tag{28}$$

As r_{sw} is twice continuously differentiable, so are $\boldsymbol{B}$ and $\boldsymbol{S}$.

To proceed further, several results from vector calculus are needed. Suppose $C(s)$ is a space curve parameterized by s, the position along the curve from some point s_0, which can be represented by a vector function $\boldsymbol{C} = \boldsymbol{C}(s)$. From standard books on vector calculus or differential geometry (Struik 1988) it can be found that differentiating $\boldsymbol{C}(s)$ with respect to the position s gives a unit vector $\hat{t}_C$ which is tangent to C at s. That is,

$$\frac{d}{ds}\boldsymbol{C}(s) = \hat{t}_C \tag{29}$$

A second result is one of Frenet's formulas and relates the derivative of the unit tangent

vector to the unit normal by

$$\frac{d}{ds}\hat{t}_C = K_C\hat{n}_C\,, \tag{30}$$

where K_C is the curvature. It will be most convenient, in the case of the boundary, to choose one sense for the normal and then allow K_C to be either positive or negative. One additional expression relating the derivative of the unit normal and the unit tangent, also one of Frenet's formulas, is needed. It is

$$\frac{d}{ds}\hat{n}_C = -K_C\hat{t}_C\,. \tag{31}$$

This particular form follows from the more general equation when C lies in a plane, in which case there is no Torsion, and (31) results.

With the sense of ∂A_k and $\hat{n}_B$ predetermined, a positively oriented unit tangent to $\dot{B}$, $\hat{t}_B$, will be as shown in Figure 19. The curvature along B is denoted K_B and may be positive or negative. For the skeleton segment S_B, the orientation of the unit tangent $\hat{t}_S$ and unit normal $\hat{n}_S$ are chosen so that $\hat{t}_S \circ \hat{t}_B \geq 0$ (Figure 19) and so that $\hat{t}_S \times \hat{n}_S$ follows the right hand rule. The sign of the skeleton curvature K_S is chosen accordingly.

We begin by differentiating (27) with respect to w, to get

$$\begin{aligned}\frac{dr_{sw}}{dw} &= -\frac{d}{dw}((r_B\hat{n}_B)) \\ &= -\left(\frac{dr_B}{ds}\frac{ds}{dw}\hat{n}_B + r_B\frac{d}{dw}\hat{n}_B\right).\end{aligned}$$

Then, after combining that and (31) it follows that

$$\frac{dr_{sw}}{dw} = -\frac{dr_B ds}{ds\, dw}\hat{n}_B + r_B K_B \hat{t}_B . \tag{32}$$

Next, equation (28) is differentiated with respect to w yielding

$$\begin{aligned}\frac{dr_{sw}}{dw} &= \frac{dB}{dw} - \frac{dS}{dw} \\ &= \frac{dB}{dw} - \frac{dS\, ds}{ds\, dw}\end{aligned}$$

That becomes, after applying (29) to both B and S,

$$\frac{dr_{sw}}{dw} = \hat{t}_B - \frac{ds}{dw}\hat{t}_S .$$

Equating the last expression and equation (32) then gives

$$-\frac{dr_B ds}{ds\, dw}\hat{n}_B + r_B K_B \hat{t}_B = \hat{t}_B - \frac{ds}{dw}\hat{t}_S . \tag{33}$$

The first of two important expressions is obtained by taking the dot product of $\hat{n}_B$ and (33). The result is

$$\frac{dr_B}{ds} = \hat{t}_S \circ \hat{n}_B . \tag{34}$$

To obtain the second expression, $\hat{t}_B$ is first dotted into (33), giving

$$r_B K_B = 1 - \frac{ds}{dw}\hat{t}_S \circ \hat{t}_B . \tag{35}$$

Equation (34) is then differentiated with respect to w yielding

$$\frac{d^2 r_B ds}{ds^2\, dw} = \frac{d}{ds}\hat{t}_S \circ \hat{n}_B \frac{ds}{dw} + \hat{t}_S \circ \frac{d}{dw}\hat{n}_B ,$$

which, using equations ((30)) and ((31)), can be written as

$$\frac{d^2 r_B}{ds^2}\frac{ds}{dw} = K_S \hat{n}_S \circ \hat{n}_B \frac{ds}{dw} - K_B \hat{t}_S \circ \hat{t}_B .$$

Solving for $\frac{ds}{dw}$ yields

$$\frac{ds}{dw} = \frac{-K_B \hat{t}_S \circ \hat{t}_B}{\frac{d^2 r_B}{ds^2} - K_S \hat{n}_S \circ \hat{n}_B} .$$

Finally, the last expression is substituted into equation (35), along with $\hat{n}_S \circ \hat{n}_B = \hat{t}_S \circ \hat{t}_B$ (see Figure 19), and solved for the boundary curvature K_B to get,

$$K_B = \frac{\frac{d^2 r_B}{ds^2} - K_S \hat{n}_S \circ \hat{n}_B}{r_B\left(\frac{d^2 r_B}{ds^2} - K_S \hat{n}_S \circ \hat{n}_B\right) + (\hat{n}_S \circ \hat{n}_B)^2} . \tag{36}$$

It also follows from Figure 19 and equation (34) that

$$\hat{n}_S \circ \hat{n}_B = \cos\varphi = \sin\theta = \sqrt{1 - \left(\frac{dr_B}{ds}\right)^2} . \tag{37}$$

In returning to a digitized setting, assumptions regarding differentiability of r_B may not be valid. To circumvent differentiability problems with r_B, a least squares approximation is used over the interval of interest. Least squares approximations are also used to determine tangent vectors, normal vectors, and curvature at points along the skeleton.

Identification Criteria

Component parameter values are to be obtained via stereology and measurement of corresponding profiles from a surface section. Two of the profiles of interest are bond lines and neck base lines, but these features are not visible and therefore must be deduced from the surrounding ice profile. To identify profile features which correspond to bond or base lines, a set of rules are needed. This helps in maintaining consistency and objectivity during profile analysis. As a result measured component parameter values better reflect the actual average characteristics. There is also a significant reduction in the amount of bias that might potentially be associated with the identification process.

The process of making cross sections, limits information regarding surface irregularities and overall geometry. Also, how a profile relates to the particular component, of which it is a part, may not be evident. These factors need to be taken into account when analyzing a set of profiles.

Criteria which take these factors into account have been formulated for bond lines (bond profile) by Kry (1975a). These criteria state that to identify an ice profile constriction (minimum profile cross section) as a bond line, a minimum relative constriction must exist on the surface section, both edges of the ice must be notched at the constriction, and the notches must point approximately towards one another. Gubler (1978b) defined bond line cross sections to be those lines defined by every obvious pair of facing necks. In this case the neck profile is the plane intersection of $S_{\eta i}$ (Figure 17). Illustrated in Figure 20 is a typical profile that these rules would require to be present in order for a bond line to be defined. It is basically a two dimensional projection of the three dimensional definition.

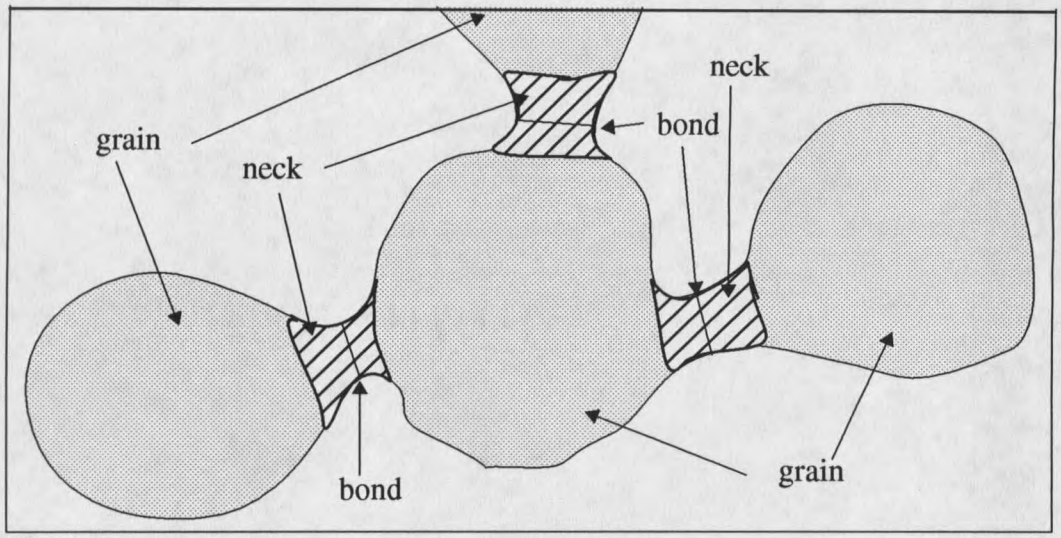

Figure 20. An ice profile partitioned into grain, neck, and bond profiles.

As stated, these rules are not well enough defined to be implemented in a clear, consistent, and objective manner (Dozier et al 1987). With the results of the last section, a precise set of rules can be stated which eliminate the subjectivity normally associated with bond and neck identification. They will be stated using skeleton related notation. This type of formulation provides a direct link to automated identification via skeleton-based automation procedures.

Let $I_{12} = (s_1, s_2)$ be a segment of a skeleton Σ_k and $r_{I_{12}}(s)$ be a twice continuously differentiable function giving the maximal disk radius at s in I_{12}. If $\frac{dr_B}{ds}$ and $\hat{t}_S$ are known at a point s in I_{12}, then equation (34) and $\hat{n}_B \bullet \hat{n}_B = 1$ can be used to determine $\hat{n}_B$. Finally, since r_B at s is known (recall it is a direct result of skeletonization) and since $\hat{n}_B$ has just been determined, equation (27) can be used to evaluate r_{sw}.

Suppose that there exists a point $s = s_0$ in I_{12} at which $r_B(s)$ attains a minimum. It follows from equation (34), that $\hat{t}_S \circ \hat{n}_B = 0$ at s_0. Let $d_{min} = 2r_B(s_0)$. If this diameter is drawn through s_0, normal to the skeleton at s_0, the area A_k is partitioned into two disjoint areas A_{k1} and A_{k2}. Let $d(A_k)$ be a linear measure of size for the area A_k (choosing $d(A_k)$ is discussed below). The diameter $d_c = d_{min}$ will be called a planar constriction of A_k if:

1) $\left(c_{r1} \equiv \frac{d_{min}}{d(A_1)}\right) < 1$, $\left(c_{r2} \equiv \frac{d_{min}}{d(A_2)}\right) < 1$,

and

2) there exists an open neighborhood δ about s_0 in which

$$\left(K_B = \frac{\frac{d^2 r_B}{ds^2} - K_S \hat{n}_S \circ \hat{n}_B}{r_B\left(\frac{d^2 r_B}{ds^2} - K_S \hat{n}_S \circ \hat{n}_B\right) + (\hat{n}_S \circ \hat{n}_B)^2} \right) < 0.$$

The planar constriction d_c of plane area A_k defines a bond line if, given an α_b, $0 < \alpha_b < 1$, both $c_{r1} \le \alpha_b$ and $c_{r2} \le \alpha_b$. Where c_{r1} and c_{r2} are the constriction ratios defined in 1 above.

The simplest definition of $d(A_k)$ is obtained by letting $d(A_1) = 2r_B(s_{m1})$, (k=1) and $d(A_2) = 2r_B(s_{m2})$, (k=2), where $r_B(s_{m1})$ and $r_B(s_{m1})$ are radii of the largest maximal disks in A_{k1} and A_{k2} respectively. This definition is the implemented by the author in a computer program based upon the results of this chapter. Because there may be more appropriate ways of defining $d(A_k)$ in some situations, it is appears in the constriction definition with no more constraint than it must be a linear size measure.

The selection of bond constriction ratio, α_b, values may vary depending, for example, upon knowledge of the ice network geometry, surface smoothness, and shape. Kry (1975a) suggested $\alpha_b = 0.7$. Gubler's (1978b) definition implicitly contains a constriction. Since he defines a bond wherever there is an "obvious neck", exactly what value of α_b that refers to is not clear though.

Once a bond profile has been identified, the corresponding neck base-plane profiles can be found. At a point s of the skeleton segment S_B the unit tangent there, $\hat{t}_S$, can have two orientations, differing only in sign (see Figure 21), depending upon the position and relative orientation of $\hat{t}_B$. Recall $\hat{t}_S$ is chosen so that $\hat{t}_S \circ \hat{t}_B \geq 0$. In accordance with the two orientations of $\hat{t}_S$ at s, there are two possible orientations of $\hat{n}_S$ at s. As a result, given a $|K_S \hat{n}_S \circ \hat{n}_B|$ at s, $K_S \hat{n}_S \circ \hat{n}_B$ can take on two values, differing only in sign. With the aid of equation (37), $K_S \hat{n}_S \circ \hat{n}_B$ can be expressed as $K_S \hat{n}_S \circ \hat{n}_B = \pm |K_S| \sqrt{1 - \left(\frac{dr_B}{ds}\right)^2}$. Substitution into equation (36) gives the two following equations:

$$K_{B1} = \frac{\frac{d^2 r_B}{ds^2} - |K_S| \sqrt{1 - \left(\frac{dr_B}{ds}\right)^2}}{r_B \left(\frac{d^2 r_B}{ds^2} - |K_S| \sqrt{1 - \left(\frac{dr_B}{ds}\right)^2} \right) + \sqrt{1 - \left(\frac{dr_B}{ds}\right)^2}} \tag{38}$$

and

$$K_{B2} = \frac{\frac{d^2 r_B}{ds^2} + |K_S|\sqrt{1-\left(\frac{dr_B}{ds}\right)^2}}{r_B\left(\frac{d^2 r_B}{ds^2} + |K_S|\sqrt{1-\left(\frac{dr_B}{ds}\right)^2}\right) + \sqrt{1-\left(\frac{dr_B}{ds}\right)^2}}. \tag{39}$$

If $\sqrt{1-\left(\frac{dr_B}{ds}\right)^2} > 0$, then $K_B = 0$ implies either $\frac{d^2 r_B}{ds^2} - |K_S|\sqrt{1-\left(\frac{dr_B}{ds}\right)^2} = 0$ or $\frac{d^2 r_B}{ds^2} + |K_S|\sqrt{1-\left(\frac{dr_B}{ds}\right)^2} = 0$ (assuming everything is bounded).

Suppose s_k^- is a point in the interval (s_b, s_{gk}) such that for all s in (s_b, s_k^-) $K_{B1}(s) < 0$ and $K_{B1}(s_k^-) = 0$. Suppose also that s_k^+ is a point in the interval (s_b, s_{gk}) such that for all s in (s_b, s_k^+) $K_{B2}(s) < 0$ and $K_{B2}(s_k^+) = 0$. The neck base profile for the area A_k (k=1,2) is defined by the line $d_{\eta k}$ joining the two points $w(s_k^-)$ and $w(s_k^+)$.

If w_{b1} and w_{b2} denote the endpoints of d_b, the two intervals defined by $\delta_1 = (w_{11}, w_{12})$ and $\delta_2 = (w_{21}, w_{22})$, that are contained in ∂A_k, are such that w_{b1} is contained in δ_1, w_{b2} is contained in δ_2, $K_B(w) < 0$ for each w in δ_1 and δ_2, and $K_B(w_{11}) = 0$, $K_B(w_{12}) = 0$, $K_B(w_{21}) = 0$, and $K_B(w_{22}) = 0$, see Figure 21 for an illustration. w_{11}, w_{21} correspond to (s_1, s_0), and w_{12}, w_{22} correspond to (s_0, s_2). The neck profile is the area bounded by $d_{\eta 1}$, $d_{\eta 2}$, δ_1, and δ_2.

The results of this section are precise bond and neck profile identification criteria which are stated in terms of an area profile's skeleton. Computer software has been devel-

oped by the author which utilizes the above formulation to automate segmentation of surface section profiles in terms of pores, grains, bonds, and necks.

In the next section, two measurement models, one for bond size, and the other for neck length will be considered.

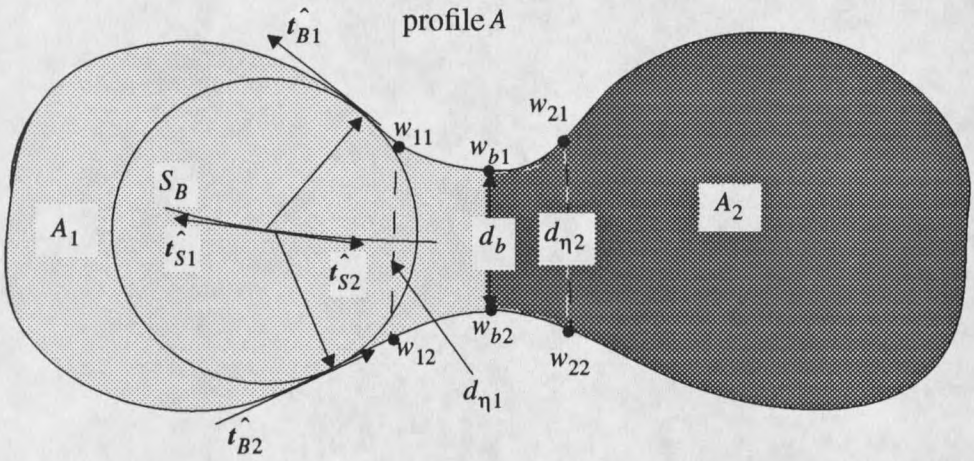

Figure 21. Profile of a bonded grain pair showing the bond line d_b and two neck base lines $d_{\eta 1}$, $d_{\eta 2}$. Also illustrated is the correspondence between two tangents $\hat{t}_{S1}$, $\hat{t}_{S2}$, at each s of S_B and the respective boundary tangents, $\hat{t}_{B1}$, $\hat{t}_{B2}$. Note: $\hat{t}_{S2} = -\hat{t}_{S1}$ and where corresponding skeleton and boundary tangents are required to satisfy $\hat{t}_S \bullet \hat{t}_B \geq 0$.

4.3 Stereology of Bonds and Necks

In this section bond and neck stereology are examined. With profiles identified and the surface section accordingly partitioned, it remains to show how the profiles can be used to measure average bond and neck parameters.

Bond plane stereology has been discussed by Kry (1975a). He made an assumption that a bond plane is approximately circular. In doing this the circular disk stereology relations of Chapter 2 become applicable. The first step in determining average bond radius is setting $d_i = d_{bi}$, where d_{bi} is the ith bond line found, in equation (22) of Chapter 2, and summing over the M bonds found. This gives the harmonic mean, $\overline{m}_b$ (equation (22)), of the bond lines. Upon substitution into (21) the average circular bond disk radius $\bar{R}_b$ is obtained. Average bond surface area, $\overline{A_b}$, is evaluated using equation (24).

It should be kept in mind that the bond planes that are identified on a section plane are only a subset of those actually intersected. For $\bar{R}_b$ to be a valid measure of average disk radius, the identified d_{bi} must have the same length probability distribution as does the entire set of intersected bond planes. Assuming random orientation, spatial distribution, and size distribution, it is reasonable to assume the length probability distributions will be the same, provided a sufficient number of bond lines are identified.

Neck Frustum

To measure average neck length, a suitable three dimensional shape needs to be specified from which stereology relations between probe measurements and parameters of interest can be determined. As will be shown later, the measurement of average neck half length can be accomplished without specifying any particular shape for the neck surface. Rather, a simple geometric shape, having the same half neck length, is assumed. The shape which will be used is the smallest closed convex surface (convex hull) formed by a

bond plane b_P, a neck base plane η_P, and the minimal surface connecting those two planes.

In order to make this approach tractable some assumptions about the general configuration of half necks are needed. In addition to the assumption of circular bond shape, three other assumptions will be made. These assumptions (notation illustrated in Figure 17) are that the neck base plane η_{Pi} is approximately circular, the surface $S_{\eta i}$ is everywhere of zero or negative curvature, and neck half length $H_{\eta i}$ joining the centers of the two planes makes a right angle with each. These immediately imply that the convex hull a half neck is a right cone frustum (Figure 22).

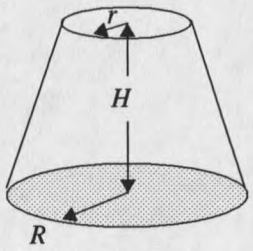

Figure 22. Right cone frustum.

By using the convex hull, measurement of neck half length is equivalent to the measurement of the height of a corresponding cone frustum. The geometric properties of a cone frustum are determined by its base radius R, its top surface radius r, and its height H (Figure 22). In the next section, the stereology relations between measurements made on planar frustum profiles and the average frustum height H are developed.

With the assumption that the neck base planes are circular disks, the average neck base plane radius and area can be evaluated using the same equations as were used to determine

mean bond radius and area. The lengths $d_i = d_{\eta i}$ of the neck base profiles (determined using the criteria of the last section) are substituted into equation (22) in order to determine the base plane profile harmonic mean $\bar{m}_\eta$. Substituting $\bar{m}_\eta$ into (21) yields the mean neck base plane radius $\bar{R}_\eta$. $\bar{A}_\eta$, the average neck base plane area, is obtained following the same procedure used to get $\bar{A}_b$.

Stereology of a Right Circular Cone Frustum

Measurement of both average bond plane and neck base plane radius were discussed earlier. In this part, stereology of a right cone frustum is developed. The result being upper and lower bounds on average length. In Figure 22 a right circular cone frustum of base radius R, top radius r, and height H is illustrated. It will be assumed that a random poly-size mixture of right circular cone frustum is being measured.

The surface area of a right cone frustum is given by

$$S = \pi(r^2 + R^2 + (r+R)\sqrt{(R-r)^2 + H^2}), \tag{40}$$

and its volume by

$$V = \frac{\pi}{3}(r^2 + R^2 + rR)H. \tag{41}$$

r, R, and H are as indicated in Figure 22.

First the average surface area and then the average volume will be examined. It is assumed that r, R, and H are independent random variables. In what follows, this implies that $\overline{rRH} = \bar{r}\bar{R}\bar{H}$, $\overline{rR} = \bar{r}\bar{R}$, $\overline{rH} = \bar{r}\bar{H}$, and $\overline{RH} = \bar{R}\bar{H}$ (see e.g. Papoulis 1991). Also used

will be the fact that the sum of the average is equal to the average of the sums. Which means, in terms of $(R+r)H$, that $\overline{(R+r)H} = \overline{RH} + \overline{rH} = \bar{R}\bar{H} + \bar{r}\bar{H}$. The surface area can be written as (over bars indicate average values, Chapter 2).

$$\bar{S} = \pi\left((\overline{r^2} + \overline{R^2}) + \overline{(r+R)\sqrt{(R-r)^2 + H^2}}\right)$$

or

$$\bar{S} = \overline{A_r} + \overline{A_R} + \overline{\pi(r+R)\sqrt{(R-r)^2 + H^2}}, \tag{42}$$

where $\overline{A_r} = \pi\overline{r^2}$ and $\overline{A_R} = \pi\overline{R^2}$.

The average volume is (recall assumption of independent random variables)

$$\bar{V} = \frac{\pi}{3}(\overline{r^2} + \overline{R^2} + \bar{r}\bar{R})\bar{H}$$

or

$$\bar{V} = \frac{1}{3}(\overline{A_r} + \overline{A_R} + \pi\bar{r}\bar{R})\bar{H}. \tag{43}$$

If average frustum volume could be estimated directly, then the last equation could, upon solving, be used to estimate $\bar{H}$. $\frac{\bar{S}}{\bar{V}}$ can be estimated though. However, $\bar{H}$ can't be factored out of equation (42). Instead, upper and lower bounds can be placed on (42) to allow an approximate solution for $\bar{H}$. The net result will then be upper and lower bounds on $\bar{H}$.

Consider first the inequality

$$R - r + H \geq \sqrt{(R-r)^2 + H^2},$$

which holds because $R \geq r$ and $H \geq 0$.

Multiplying both sides of the inequality by $R+r$ gives

$$(R+r)(R-r+H) \geq (R+r)\sqrt{(R-r)^2+H^2},$$

which, upon averaging, becomes

$$(\overline{R^2}-\overline{r^2}+(\bar{R}+\bar{r})\bar{H}) = \overline{(R+r)(R-r+H)} \geq \overline{(R+r)\sqrt{(R-r)^2+H^2}} \tag{44}$$

A lower bound follows from averaging the inequality

$$(R+r)\sqrt{(R-r)^2+H^2} \geq (R+r)H.$$

The result being

$$\overline{(R+r)\sqrt{(R-r)^2+H^2}} \geq \overline{(R+r)H} = (\bar{R}+\bar{r})\bar{H}. \tag{45}$$

Equations (42), (43), and (44) imply, after some algebra, the inequality

$$\frac{\bar{S}}{\bar{V}} \leq \frac{(2\overline{A_R}+\pi(\bar{R}+\bar{r})\bar{H})}{\frac{1}{3}(\overline{A_r}+\overline{A_R}+\pi\bar{r}\bar{R})\bar{H}}.$$

Solving for $\bar{H}$ gives the upper bound

$$\bar{H} \leq \frac{2\overline{A_R}}{\frac{1}{3}(\overline{A_r}+\overline{A_R}+\pi\bar{r}\bar{R})\frac{\bar{S}}{\bar{V}}-\pi(\bar{R}+\bar{r})}. \tag{46}$$

Combining equations (42), (43), and (45) yields the inequality

$$\frac{\bar{S}}{\bar{V}} \geq \frac{(\overline{A_r}+\overline{A_R}+\pi(\bar{R}+\bar{r})\bar{H})}{\frac{1}{3}(\overline{A_r}+\overline{A_R}+\pi\bar{r}\bar{R})\bar{H}}.$$

Solving this for $\bar{H}$ gives the lower bound

$$\bar{H} \geq \frac{\overline{A_r} + \overline{A_R}}{\frac{1}{3}(\overline{A_r} + \overline{A_R} + \pi\bar{r}\bar{R})\frac{\bar{S}}{\bar{V}} - \pi(\bar{R} + \bar{r})}. \tag{47}$$

Evaluation of (46) and (47) requires estimates of $\bar{r}$, $\bar{R}$, $\overline{A_r}$, $\overline{A_R}$, and $\frac{\bar{S}}{\bar{V}}$. Which, stated in terms of bond and neck parameters, requires estimates for $\bar{r} = \overline{R_b}$, $\bar{R} = \bar{R}_\eta$, $\overline{A_r} = \overline{A_b}$, and $\overline{A_R} = \overline{A_\eta}$. Estimating these parameters has already been discussed.

From Chapter 2 it follows that $\left(\frac{\bar{S}}{\bar{V}}\right)_{cf} = \frac{2P_L(cf)}{L_L(cf)}$, where $P_L(cf)$ is the number of frustum profile boundary intercepts and $L_L(cf)$ is the linear fraction of the frustum profiles. One problem exists with using the convex hull. Its free surface, corresponding to $S_{\eta i}$, is a modeling construct and therefore is not necessarily a physically realized surface. As with bond profiles, its intersection profile must be inferred from visible profiles. Because the profiles which would be generated vary in shape, and are unknown, an approximation will be used. The approximation made is a trapezoid T_f formed by joining the ends of a bond line d_b and neck base line d_η, as illustrated by the cross hatched area in Figure 23. $P_L(T_f)$ and $L_L(T_f)$ can now be measured for T_f.

The remainder of this part is used to examine the error in $\left(\frac{\bar{S}}{\bar{V}}\right)_{cf}$ for the frustum, incurred when approximating its cross section by a trapezoid. To begin, write

$$P_L(cf) = P_L(T_f) + \Delta P_L$$

and

$$L_L(cf) = \frac{L(T_f) + \Delta L}{L} .$$

Then $\frac{1}{2}\left(\frac{\bar{S}}{\bar{V}}\right)_{cf}$ becomes

$$\frac{1}{2}\left(\frac{\bar{S}}{\bar{V}}\right)_{cf} = \frac{P_L(T_f) + \Delta P_L}{L_L(T_f) + \Delta L_L} = \frac{P_L(T_f) + \Delta P_L}{L_L(T_f)}\left(1 + \frac{\Delta L_L}{L_L(T_f)}\right)^{-1}$$

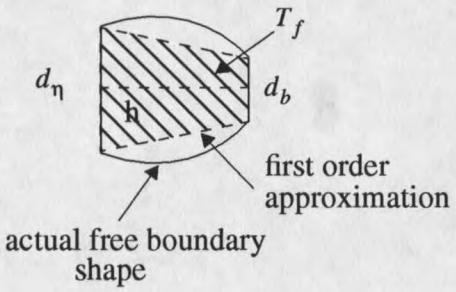

Figure 23. Top view of a frustum cross section. Necked regions generally have a concave profile rather than the convex shape shown.

This ratio can be expanded using the binomial expansion, assuming $\left(\frac{\Delta L_L}{L_L(T_f)}\right)^2 < 1$, and gives

$$\frac{P_L(T_f) + \Delta P_L}{L_L(T_f)}\left(1 + \frac{\Delta L_L}{L_L(T_f)}\right)^{-1} \cong \frac{P_L(T_f) + \Delta P_L}{L_L(T_f)}\left(1 - \frac{\Delta L_L}{L_L(T_f)} + \left(\frac{\Delta L_L}{L_L(T_f)}\right)^2 - \ldots\right) .$$

To first order then,

$$\frac{1}{2}\left(\frac{\bar{S}}{\bar{V}}\right)_{cf} \cong \frac{P_L(T_f) + \Delta P_L}{L_L(T_f)}\left(1 - \frac{\Delta L_L}{L_L(T_f)}\right)$$

$$\frac{1}{2}\frac{\bar{S}}{\bar{V}} \cong \frac{P_L(T_f)}{L_L(T_f)} + \frac{\Delta P_L}{L_L(T_f)} - \frac{P_L(T_f)}{L_L(T_f)}\frac{\Delta L}{L(T_f)}$$

$$\frac{1}{2}\frac{\bar{S}}{\bar{V}} \cong \frac{P_L(T_f)}{L_L(T_f)} + \frac{\Delta P}{L(T_f)} - \frac{P(T_f)}{L(T_f)}\frac{\Delta L}{L(T_f)}. \tag{48}$$

ΔP_L measures only those curved frustum boundary-profile intercepts which do not pass through the trapezoid portion of a frustum profile. If the curved boundaries do not extend too far from the straight trapezoid side, ΔP_L is likely to be close to zero implying $\Delta P_L \ll P_L(T_f)$. Equation (48) simplifies to

$$\frac{1}{2}\frac{\bar{S}}{\bar{V}} \cong \frac{P_L(T_f)}{L_L(T_f)}\left(1 - \frac{\Delta L}{L(T_f)}\right). \tag{49}$$

Identification of bonds and necks is restricted to those that, when intersected, also happen to lay in a favorable orientation. Also, the intersected bond and neck planes must be part of a connected ice profile. As such, orientations of the associated neck frustum symmetry axis are not likely to be inclined at any large angle with respect to the section plane. This greatly limits the deviations of the approximate section trapezoids from a true frustum profile. As a result it is reasonable to suggest that in general $\frac{\Delta L}{L(T_f)} \ll 1$. That and equation (49) then indicate that the error induced by approximating the neck frustum cross sections as trapezoids should typically be negligible.

CHAPTER 5

MICROSTRUCTURE EVOLUTION

Theoretical studies of snow metamorphism lack a comprehensive set of experimental results for which extensive measurement of microstructure have been conducted. As mentioned in Chapter 1, another problem is that most theoretical works tend to model grains as spheres. The measurements presented in what follows are intended to be a start in addressing these needs. They are also important for showing that objective bond and neck based analysis of surface sections can be achieved by applying the skeleton methods of Chapter 3 and the developments of Chapter 4.

The experimental study presented below allowed spherical ice grains to metamorphose for varying periods of time and at one of four temperatures. In the next section this experiment is described. Following that, the results of the microstructure analysis are presented (section 5.2). In the last section (5.3), a brief discussion of the dependence of analysis results on the choice of bond constriction ratio is presented.

5.1 Experiment

In this experiment, aggregates of spherical ice particles were allowed to undergo natural microstructure induced metamorphism. Production of ample quantities of spherical ice

particles was accomplished using a device developed in Japan. One of these was brought to the Cold Regions Lab, here at Montana State University, in 1995 by Dr. Atsushi Sato. Ice particles are formed by spraying a fine water mist into the top end of a dry ice tunnel (Sato et al. 1996). As water droplets from the mist fall downward through the tunnel, they freeze. The size of the ice particles can be varied by adjusting the size of the water droplets. During operation dry ice tunnels usually lasted between 10 and 20 minutes. That placed a limit on the quantity of ice-grains that could be produced. Since the ice particles were to be placed in several sample trays, the trays were placed at the bottom in a bowl, which in turn was placed at the exit of the dry ice tunnel. In this way ice particles were deposited directly into the sample trays.

Twelve aluminum sample trays, 3.8x3.8x1.9 cm, were used for each experimental run. Over the particle production time, collection depths were between 4 and 6 mm. The average radius of the newly formed ice-grains was $R_g \approx 22\ \mu m$. In order to complete the sample preparation, the sample trays were carefully removed from the collection bowl. In order to completely fill the trays, any material remaining in the collection bowl was slid out and onto the partially filled trays. Material extending above the tray was left intact, so as not to disturb the consolidating mass any further.

Excess material was placed, along with the trays, into a plastic zip-lock bag. Before sealing, the bag was pressed in order to remove as much excess air as possible. The bag was then sealed. The same procedure was followed each time the bag was opened to allow removal of a single sample.

Each of three test sets were kept in a cold room at one of three temperatures (-15±1°C, -10±1°C, -5±1°C). A fourth set was placed in a smaller freezer set to -2°C. Because the air temperature of the small freezer varied by ±6°C, the samples and sealed bag were placed within a foam box which was partially filled with natural snow and plastic ice packs. This reduced the temperature oscillations to less than ±1°C. At pre-selected time intervals, a sample was removed from the sealed bag. A pore filler of Dimethy-pthalate, at temperature between -4 and -2°C, was then pored into the sample. Once filled (no attempt was made to trim material above the trays) the filler was allowed to freeze. The process was repeated at time intervals of 0, 1, 3, 6, 9, 12, 24, 48, 72, 168, 336, and 840 hours.

After a filled sample had solidified, an aluminum pedestal was placed (room temperature) onto the exposed part of the sample. Solidified samples were removed from the trays by first holding the metal parts in bare hands. This melted a very thin layer between the sample and tray. The solid could then be coaxed out by tapping the bottom. The surface was allowed to refreeze. Each sample was then placed into individual zip-lock plastic bags and labeled.

To prepare a "stopped" (filler in place and solidified) sample for analysis, several mm were shave off of the now exposed bottom surface using a sharp wood plane. This exposed surface was gently polished with a paper cloth and then allowed to sit for fifteen minutes (Perla 1982). Lamp Black powder was applied to the surface which was then polished. Occasionally several applications were needed. The final result was a surface on which lamp black was adhered to the exposed ice surface but not to the pore filler surface.

Finally, each polished sample was placed under a microscope for image recording. A 256 gray level CCD camera attached to the microscopes camera port was used to record the images digitally. An attempt was made to strike a balance between a statistically adequate number of particles appearing within an image frame and between resolution. Other than the run at -15°C, two different magnifications were used. The switch usually occurred around the third day of the test (as indicated in Table 1). At each change in magnification, a ruled glass micrometer scale was photographed for later reference. Table 1 lists pixel resolutions (in mm), magnification factors, and analysis areas (mm^2). They are grouped by the first time (hours) of that part of the time series sequence to which those values apply. They hold for each successive time step up until a switch occurred at the second indicated time.

Temperature (^oC)	First Hour of Series	Resolution (mm)	Magnification	Image Area (mm^2)	Resolution (mm)	First Hour of Series	Magnification	Image Area (mm^2)
-2	0	0.0014	7.27	0.5757	0.0034	72	2.96	3.4863
-5	0	0.0010	9.5	0.3371	0.0027	72	3.6	2.3757
-10	0	0.0015	6.62	0.6938	0.0028	72	3.52	3.3565
-15	0	0.0014	7.27	0.5757	0.0011	840	9.11	0.5737

Table 1. Pixel resolution, magnifications, and image areas for each temperature/time series. Only the first hour of a series which has the indicated statistics is listed.

Section-planes were considerably larger than the selected image frame. Normally from 6 to 12 frames, selected arbitrarily, were recorded for each section (one section plane per sample).

The last step prior to analysis of each section image was filtering and enhancement. Filtering was used to remove general background noise and to highlight grain-pore boundaries. Once grain-pore interface contrast was sufficiently enhanced, these were traced. Thresholding then left only the boundary. The interior regions of these boundaries were then filled. Because this process is so time consuming, images were only prepared for the time intervals, 0, 12, 24, 72, 168, 336, and 840 hours. Note that last time recorded for the -5°C was not 840 hours but rather 1080 hours. Of those time intervals, at least five images were selected for analysis. The selection was determined by the anticipated ease with which an image might be accurately converted to binary, i.e. images had good grain-pore interface and had the fewest ambiguous boundaries. Figure 24 shows a part of a surface section as it appears in binary form.

5.2 Surface Section Analysis Results

Over 160 surface sections were made ready for analysis. Illustrated in Figure 24 is a sub-area from one of these binary images. A micrometer ruler is shown for reference. Initially, each binary image, such as Figure 24, was analyzed to obtain ice area fractions $A_A(\iota)$ as well as the specific ice surface area $S_V(\iota)$ (relative to the sample volume). $A_A(\iota)$ is the fraction of pixels corresponding to ice on a binary image (black). Generally volume fractions were between 0.42 and 0.50 as indicated in Table 2. The average values are very consistent (0.47 to 0.52) for the -2°C. The others are much less stable in this regard. That these don't show a definite decrease over time indicates that mass loss is probably not to